BJP BRITISH JOURNAL OF PHARMACOLOGY

BPS BRITISH PHARMACOLOGICAL SOCIETY

British Journal of Pharmacology (2010), ••, ••–••

0007-1188/10
www.brjpharmacol.org

RESEARCH PAPER

Nicotinic acetylcholine receptors expressed in the ventralposterolateral thalamic nucleus play an important role in anti-allodynic effects

M Ueda[1,2], Y Iida[3], A Tominaga[2], T Yoneyama[2], M Ogawa[4], Y Magata[4], H Nishimura[5], Y Kuge[2]* and H Saji[2]

[1]*Radioisotopes Research Laboratory, Kyoto University Hospital, Faculty of Medicine, Kyoto University, Kyoto, Japan,* [2]*Department of Patho-Functional Bioanalysis, Graduate School of Pharmaceutical Sciences, Kyoto University, Kyoto, Japan,* [3]*Bioimaging Information Analysis, Graduate School of Medicine, Gunma University, Maebashi, Japan,* [4]*Laboratory of Genome-Bio Photonics, Photon Medical Research Center, Hamamatsu University School of Medicine, Hamamatsu, Japan, and* [5]*Radioisotope Laboratory, Kyoto Prefectural University of Medicine, Kyoto, Japan*

Background and purpose: Much interest is currently being focused on the anti-nociceptive effects mediated by nicotinic acetylcholine (nACh) receptors, including their location and mechanism of action. The purpose of this study was to elucidate these issues using 5-iodo-3-(2(S)-azetidinylmethoxy)pyridine (5IA), a nACh receptor agonist, and [^{125}I]5IA.
Experimental approach: We partially ligated the sciatic nerve of Sprague-Dawley rat to induce neuropathic pain [Seltzer's partial sciatic nerve ligation (PSL) model]. We then examined the changes in nACh receptor density in the CNS using [^{125}I]5IA autoradiography and the involvement of nACh receptors in anti-nociceptive effects in the region where changes occurred.
Key results: Autoradiographic studies showed that the accumulation of [^{125}I]5IA and the number of nACh receptors in the thalamus of PSL rats were increased about twofold compared with those in the sham-operated rats. No change was observed in other brain regions. Rats injected in the ventral posterolateral thalamic nucleus (VPL) with 5IA demonstrated a significant and dose-dependent anti-allodynic effect and this effect was completely antagonized by mecamylamine, injected with 5IA, into the VPL. The blockade of nACh receptors in the VPL by mecamylamine decreased by 70% the anti-allodynic effect of 5IA, given i.c.v. Moreover, mecamylamine given intra-VPL by itself, induced significant hyperalgesia.
Conclusions and implications: Our findings suggest that the nACh receptors expressed in the VPL play an important role in the anti-allodynic effects produced by exogenous and endogenous agonists.
British Journal of Pharmacology (2010) doi:10.1111/j.1476-5381.2009.00613.x

Keywords: nicotinic acetylcholine receptor; thalamus; ventral posterolateral thalamic nucleus; 5IA; anti-allodynic effect; neuropathic pain

Abbreviations: 5IA, 5-iodo-3-(2(S)-azetidinylmethoxy)pyridine; MPE, maximal possible effect; nACh, nicotinic acetylcholine; NRM, nucleus raphe magnus; PPTg, pedunculopontine tegmental nucleus; VPL, ventral posterolateral thalamic nucleus

Introduction

Numerous studies have shown that nicotinic acetylcholine (nACh) receptor agonists possess analgesic effects (Decker *et al.*, 2004; Jain, 2004). Because these effects are not antagonized by opioid receptor antagonists and arise from the activation of nACh receptors (Bannon *et al.*, 1998a; nomenclature follows Alexander *et al.*, 2008), much interest has been focused on nACh receptors as a novel target of anti-nociceptive drugs that do not involve the opioid system. Although morphine is a very well known and effective analgesic, its usefulness for patients with neuropathic pain is limited (Bannon *et al.*, 1998c; Sindrup and Jensen, 1999). In contrast, nACh receptor agonists are able to ameliorate neuropathic pain by affecting systems other than the opioids (Bannon *et al.*, 1998b,c; Decker *et al.*, 1998). Therefore,

Correspondence: Hideo Saji, Department of Patho-Functional Bioanalysis, Graduate School of Pharmaceutical Sciences, Kyoto University, 46-29 Yoshida Shimoadachi-cho, Sakyo-ku, Kyoto 606-8501, Japan. E-mail: hsaji@pharm.kyoto-u.ac.jp
*Present address: Central Institute of Isotope Science, Hokkaido University, Sapporo 060-0815, Japan.
Received 24 April 2009; revised 22 July 2009; accepted 18 October 2009

identification of the sites of action of nACh receptor agonists and the elucidation of their anti-allodynic mechanisms are desirable.

One of the most studied nACh receptor-acting analgesics is ABT-594. This compound is a selective and potent agonist with high affinity for α4β2-nACh receptors (predominant in the brain), low affinity for α7-nACh receptors and no affinity for α1β1γδ-nACh receptors (Donnelly-Roberts *et al.*, 1998; Holladay *et al.*, 1998). By virtue of this selectivity, ABT-594 has analgesic efficacy with an improved therapeutic window compared with non-selective agonists such as epibatidine (Bannon *et al.*, 1998b).

Recently, 5-iodo-3-(2(S)-azetidinylmethoxy)pyridine (5-iodo-A-85380, 5IA), an analogue of ABT-594, was synthesized (Saji *et al.*, 2002). It is also an α4β2-nACh receptor-specific agonist (Ueda *et al.*, 2008) with a relatively good safety profile (Vaupel *et al.*, 2003; Ueda *et al.*, 2004). In addition, radiolabelled 5IA, [$^{123/125}$I]5IA, was also developed (Saji *et al.*, 2002) and was reported to be a promising ligand for imaging nACh receptors in rodents and in humans (Saji *et al.*, 2002; Mamede *et al.*, 2004; Mamede *et al.*, 2007; Oishi *et al.*, 2007; Brasic *et al.*, 2009). Non-radioactive 5IA and [$^{123/125}$I]5IA can be considered the same compound with regard to their biodistribution or metabolism. Therefore, the pharmacokinetics, receptor occupancy and binding potential (an index of nACh receptor density) of 5IA are able to be measured readily using [$^{123/125}$I]5IA. Studies using 5IA have the advantage that pharmacodynamic effects can be compared directly with the pharmacokinetic profile of the compound.

Previous studies have demonstrated the up-regulation of spinal muscarinic acetylcholine receptors (Chen and Pan, 2003) and thalamic cannabinoid CB_1 receptors (Siegling *et al.*, 2001) in neuropathic pain models. It has been reported that the up-regulation of muscarinic and CB_1 receptors contributes to the increased analgesic efficacy of each agonist. As nACh receptor agonists are also effective against neuropathic pain, up-regulation of nACh receptors may also occur in such models. We hypothesized that brain regions where changes in the density or function of nACh receptors occurred would play an important role in anti-nociceptive effects, provided that such changes were found under neuropathic conditions. In the present study, we used a partial sciatic nerve ligation (PSL) model of neuropathic pain (Seltzer *et al.*, 1990) and examined the changes in nACh receptors in the PSL rats using [^{125}I]5IA. Furthermore, based on the result, we investigated the involvement of the nACh receptors expressed in the region where changes occurred as a result of the model of neuropathic pain.

Methods

Animals

Animal care and experimental procedures were conducted in accordance with our institutional guidelines, and the experimental procedures were approved by the Kyoto University Animal Care Committee.

Male Sprague-Dawley rats weighing 200–250 g were purchased from Japan SLC Co., Ltd. (Hamamatsu, Japan). The rats were kept at a constant ambient temperature under a 12 h light/dark cycle with free access to food and water.

Surgical operation

The PSL neuropathic pain model was established according to a previously published method (Seltzer *et al.*, 1990). Under sodium pentobarbital (50 mg·kg^{-1}, i.p.) anesthesia, the right sciatic nerve was exposed just distal to the branch leading to the posterior biceps femoris/semitendinosus muscles. A 7–0 silk suture was inserted into the nerve and tightly ligated so that the dorsal 1/3–1/2 of the nerve was trapped in the ligature. In the sham-operated rats, the sciatic nerve was exposed, but was left intact.

After recovery from the surgery, the rats were implanted with stainless steel guide cannulae (o.d. 0.7 mm, i.d. 0.38 mm) under sodium pentobarbital (50 mg·kg^{-1}, i.p.) anesthesia for i.c.v. or intra-ventral posterolateral thalamic nucleus (VPL) administration. The rats were placed into a stereotaxic apparatus (SR-5, Narishige Co., Ltd., Tokyo, Japan) and unilaterally implanted with a guide cannula above the lateral ventricle (0.8 mm posterior and 1.5 mm lateral to bregma, 2.0 mm below the outer surface of the skull) for i.c.v. administration or above the left VPL, which was contralateral to the nerve ligation (2.4 mm posterior and 3.3 mm lateral to bregma, 2.0 mm below the outer surface of the skull) for intra-VPL administration. The stereotaxic coordinates were determined following an atlas (Paxinos and Watson, 2005). The guide cannulae were held firmly in place using dental acrylic cement. After surgery, the rats were individually returned to their cages and left to recover for 5 days or more until the experiments.

von Frey filament test

Just before and 2 weeks after the PSL, tactile sensitivity was measured by the up-down method using calibrated von Frey filaments ranging from 0.07 to 26 g (North Coast Medical, Morgan Hill, CA, USA), in a previously described method with slight modifications (Marcil *et al.*, 2006). Briefly, for testing, the rats were individually placed on an elevated wire mesh floor. After a habituation period of 15–30 min, the tactile stimulus was applied to the middle plantar area of the each paw by placing the von Frey filament perpendicular to the surface of the paw. The filament was held in this position with enough force to cause slight bending. Each trial involved 10 applications of filaments every 1–2 s. The threshold was determined as the filament of the lowest stiffness at which the rat responded (quick paw flick) in one or more of the trial. The rats that showed a lower threshold postoperatively than preoperatively in both paws were considered as demonstrating allodynia and were used in the following studies.

Effect of 5IA and/or mecamylamine on tactile allodynia

For i.c.v. administration, an injection cannula (o.d. 0.35 mm, i.d. 0.18 mm) was inserted 5.0 mm below the surface of the skull along the guide cannula. Then, various concentrations of 5IA (1–10 nmol in 5 μL) or vehicle were infused at 5 μL per rat with a constant rate of 10 μL·min^{-1} using a microsyringe

pump (EP-60; Eicom Corporation, Kyoto, Japan). The cannula was retained in place for an additional 1 min to prevent backflow of the drugs. When required, mecamylamine (5 $mg \cdot kg^{-1}$) was injected subcutaneously 30 min before i.c.v. administration of 5IA.

For intra-VPL administration, an injection cannula was inserted 6.2 mm below the surface of the skull. Subsequently, vehicle, 5IA (1–50 nmol in 0.5 μL), mecamylamine (1–10 nmol in 0.5 μL) or a mixed solution of 5IA and mecamylamine (10 nmol each in 0.5 μL) was infused at 0.5 μL per rat with a constant rate of 0.4 $\mu L \cdot min^{-1}$. The cannula was retained in place for an additional 1 min.

For double injections, the cannula for intra-VPL administration was inserted intra-VPL, and mecamylamine (10 nmol in 0.5 μL) or vehicle was infused in the same way as described above. Five minutes later, the cannula for i.c.v. administration was inserted, and 5IA (10 nmol in 5 μL) or vehicle was infused as described above. Both cannulae were retained in place for an additional 1 min.

Just before and 15, 30, 60, 90 and 120 min after administration, tactile allodynia was evaluated using the von Frey filament test. The results were expressed as a percentage of the maximal possible effect (% MPE) according to the following formula:

$$\%MPE = \frac{\text{post-drug threshold} - \text{pre-drug threshold}}{\text{cut-off (26 g)} - \text{pre-drug threshold}} \times 100$$

Inclined plane test

The inclined plane test was carried out using a sliding apparatus (Medical Agent Co., Ltd., Kyoto, Japan), as described previously (Okada *et al.*, 2002). This procedure was used to evaluate the effects of anti-allodynic drugs on motor function (Fukui *et al.*, 2001; Okada *et al.*, 2002; Yasuda *et al.*, 2005). Intraperitoneal administration of baclofen, which causes muscle relaxation, significantly reduced the slope angle at which rats were no longer able to maintain their position and slid down the table, thus indicating the appropriateness of this procedure (Fukui *et al.*, 2001). Each rat was placed on a stainless steel plate inclined at 30°, and the angle of the plate was increased at a rate of $2° \cdot s^{-1}$. The maximum angle of the plane at which the rat maintained its body position without sliding down was determined.

The rats were habituated to the procedure three times per day. After 2 days of habituation, the test was performed three times, and the mean of the last two values was taken as a control. Soon after measuring the control value, drugs or vehicle were administered via each route, as described above, and the maximum angle before sliding down was determined at 15, 30, 60, 90 and 120 min after administration. Drugs were used at the maximum concentration for each administration route. The data are represented as a percentage of the control value.

Ex vivo *autoradiography*

Ex vivo autoradiography was performed using a previously described method (Kanegawa *et al.*, 2006) with slight modifications. Three groups of rats, a sham-operated group, a 2 week and a 1 month post-PSL group, were used in this experiment. Each group consisted of four to seven animals.

Each rat was injected with 2 MBq of [^{125}I]5IA via its tail vein and killed 60 min after radioligand injection. Their brains were quickly removed, frozen in hexane (–80°C) and cut into 20 μm-thick coronal sections with a cryomicrotome (CM3000, Leica, Germany). The sections were exposed to imaging plates (BAS-UR, Fuji Photo Film Co., Ltd., Tokyo, Japan) with ^{125}I autoradiographic microscale standards (Amersham Biosciences, Buckinghamshire, UK). After 25 h exposure, the [^{125}I]5IA autoradiograms were obtained using a bioimaging analyzer (BAS 3000, Fuji Photo Film Co., Ltd., Tokyo, Japan), and quantitative densitometric analyses were performed with dedicated software (Image Gauge ver. 3.1, Fuji Photo Film Co., Ltd., Tokyo, Japan). Regions of interest were drawn over eight brain regions bilaterally [frontal cortex, striatum, hippocampus, thalamus, pedunculopontine tegmental nucleus (PPTg), nucleus raphe magnus (NRM), locus coeruleus and cerebellum]. Data were represented as the mean of the ligated and contralateral side.

In vitro *autoradiography*

Three groups of rats were used as described for the *ex vivo* autoradiography. Each group consisted of five to seven animals. The rats were killed and their brains were removed and frozen immediately. Each frozen brain was cut into 20 μm-thick coronal sections, thaw-mounted onto gelatin-coated glass slides and kept frozen at –80°C until use.

A method for the autoradiographic determination of receptor density was previously published (Tanaka *et al.*, 1993; Suzdak *et al.*, 1994). A binding assay was conducted using a modification of a previously described method (Mukhin *et al.*, 2000). The assay buffer used was 50 mM Tris-HCl (pH 7.0) containing 120 mM NaCl, 5 mM KCl, 2.5 mM $CaCl_2$ and 1 mM $MgCl_2$. The sections were incubated with 23.75–380 pM [^{125}I]5IA (specific activity: 220 $Ci \cdot mmol^{-1}$) in the same buffer for 1 h at 25°C, then rinsed twice in ice-cold buffer for 5 min each time, and once in distilled water for 1 min, and dried under a cold air stream. Non-specific binding was determined in the presence of 300 μM (–)-nicotine. The sections were exposed to the imaging plates with ^{125}I standards for 20 h. The autoradiograms were obtained and the quantitative analyses were performed in a similar way to that described above. Values for the maximum density of binding sites (B_{max}) were gained from saturation binding isotherms (one-site binding) of specific binding by means of nonlinear curve fitting (Prism 5.00, GraphPad Software, San Diego, CA, USA).

Statistical analyses

After the behavioural experiments, the rats were killed, and their brains were removed and frozen immediately. Coronal sections (20 μm) including the VPL were prepared and thaw-mounted onto gelatin-coated glass slides and subjected to Nissl staining. The placements of the tips of the injection cannulae were confirmed by using the atlas (Paxinos and Watson, 2005). Only data from rats with the injection cannulae correctly placed in the VPL were used for the statistical analyses.

The analyses of the data from the von Frey filament test and the inclined plane test were performed using two-way analysis of variance (ANOVA) with repeated measures. If there was a significant difference, a *post hoc* one-way ANOVA followed by a Tukey-Kramer multiple comparison test was performed using each treatment combination as an independent group. Analyses of the data from the autoradiographic studies were performed using a one-way ANOVA followed by a Tukey-Kramer multiple comparison test. Differences were considered significant when $P < 0.05$.

Materials

5IA and [^{125}I]5IA were synthesized according to a previously published method (Saji *et al.*, 2002). Mecamylamine hydrochloride, a nACh receptor antagonist, was purchased from Sigma-Aldrich (St. Louis, MO, USA). The sodium pentobarbital for injection was purchased from Dainippon Sumitomo Pharma Co., Ltd. (Osaka, Japan). All drugs were administered in physiological saline solution. All other chemicals used were of reagent grade.

Results

Anti-allodynic effect of i.c.v. administered 5IA

In the present study, the rats presented a bilateral tactile allodynia following the PSL. The paw withdrawal thresholds decreased from 13.4 ± 0.9 g to 3.1 ± 0.3 g and from 13.4 ± 1.0 g to 4.2 ± 0.4 g in the ligated paws and the contralateral paws respectively. First, we evaluated an anti-allodynic effect of i.c.v. administered 5IA, as there has been no previous report regarding whether 5IA is able to palliate neuropathic pain. Figure 1A shows the anti-allodynic effect observed in the ligated paws. Two-way ANOVA demonstrated significant main effects of treatment ($F_{3,90} = 5.56$, $P = 0.007$) and time ($F_{4,90} = 7.51$, $P < 0.001$) and a significant interaction between treatment and time ($F_{12,90} = 2.85$, $P = 0.003$). Injection of 5IA (10 nmol) increased % MPE values significantly at 15 min after administration (Vehicle: −3.4 ± 2, 10 nmol: 38 ± 6). Although the effect peaked at 15 min after administration and decreased gradually, significant increases in % MPE values were also observed in the 3 nmol- and 10 nmol-treated groups 30 min after administration. Similar results were also observed in the contralateral paws (data not shown).

Next, we examined an effect of mecamylamine, a blood–brain barrier permeable nACh receptor antagonist, on the anti-allodynic effect of 5IA. Significant main effects of treatment ($F_{3,95} = 6.75$, $P = 0.003$) and time ($F_{4,95} = 5.61$, $P < 0.001$) and a significant interaction between treatment and time ($F_{12,95} = 7.44$, $P < 0.001$) were found. Mecamylamine (5 mg·kg^{-1}, s.c.) blocked the effect of 5IA completely and the % MPE values were reduced to levels obtained after treatment with vehicle (Figure 1B).

Changes in the accumulation of [^{125}I]5IA in vivo

We compared [^{125}I]5IA accumulation between the PSL model rats and the sham-operated rats using an *ex vivo* autoradiographic method. Representative autoradiograms are shown in Figure 2A. The thalamic signals of the PSL groups were stronger than those of the sham-operated group, while the cortical and hippocampal signals were similar among the three groups. There was no difference between the ligated and contralateral sides of the PSL model rats. A significant increase (170%) in the accumulation of [^{125}I]5IA was observed only in the thalamus in both PSL groups and no detectable change was seen in other regions (Figure 2B).

Measurement of the density of nACh receptors in vitro

We performed an autoradiographic saturation assay using [^{125}I]5IA as a radioligand. The saturation binding curves are

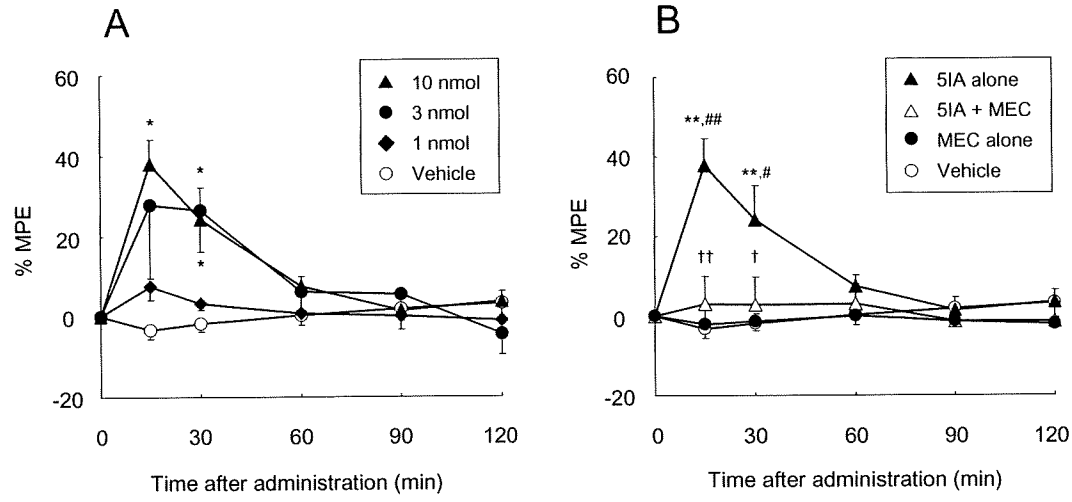

Figure 1 (A) Effect of i.c.v. administered 5IA on neuropathic tactile allodynia. Data are presented as a percentage of the maximum possible effect (% MPE). Each point represents the mean ± SEM of the ligated paws of five to six animals per group. *$P < 0.05$ versus vehicle at the same time point. (B) Effect of mecamylamine (MEC, 5 mg·kg^{-1}, s.c., 30 min prior) on the anti-allodynic effect induced by 5IA (i.c.v.). Data are presented as a percentage of the maximum possible effect. Each point represents the mean ± SEM of the ligated paws of five to six animals per group. **$P < 0.01$ versus vehicle, #$P < 0.05$, ##$P < 0.01$ versus MEC alone, and †$P < 0.05$, ††$P < 0.01$ versus 5IA alone at the same time point. 5IA, 5-iodo-3-(2(S)-azetidinylmethoxy)pyridine; MPE, maximal possible effect.

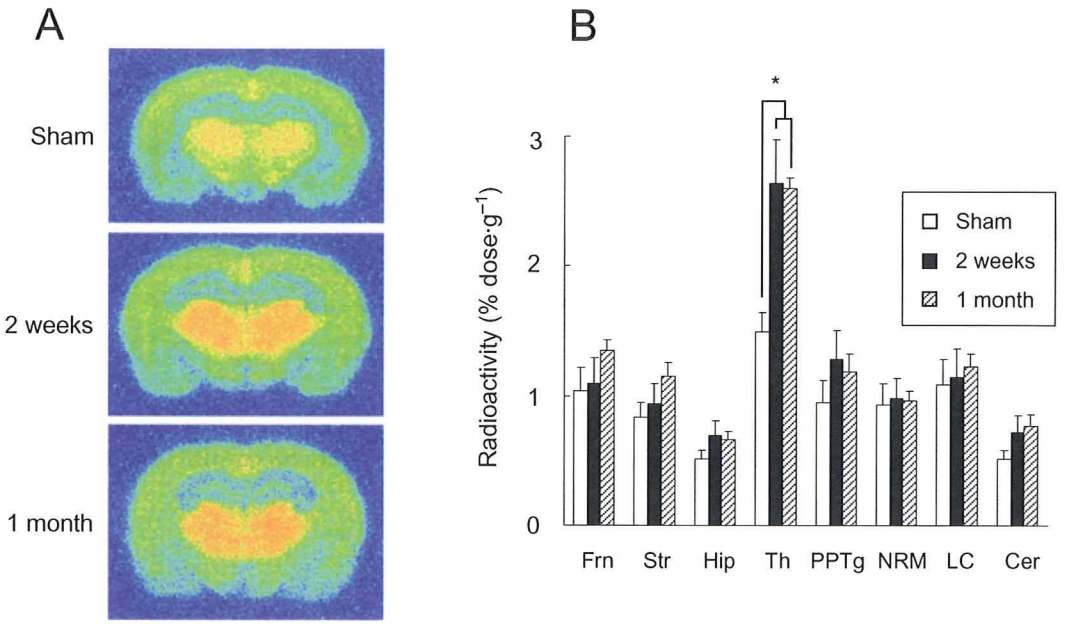

Figure 2 (A) Representative autoradiograms of brain regions from sham-operated and PSL rats given [^{125}I]5IA, i.v. (B) Changes in the regional accumulation of [^{125}I]5IA in Seltzer's PSL model of neuropathic pain. A significant increase was observed only in the thalamus, and no detectable change occurred in other regions. Each column represents the mean ± SEM of four to seven animals per group. *$P < 0.05$ versus sham. PSL, partial sciatic nerve ligation; 5IA, 5-iodo-3-(2(S)-azetidinylmethoxy)pyridine; Frn, frontal cortex; Str, striatum; Hip, hippocampus; Th, thalamus; PPTg, pedunculopontine tegmental nucleus; NRM, nucleus raphe magnus; LC, locus coeruleus; Cer, cerebellum.

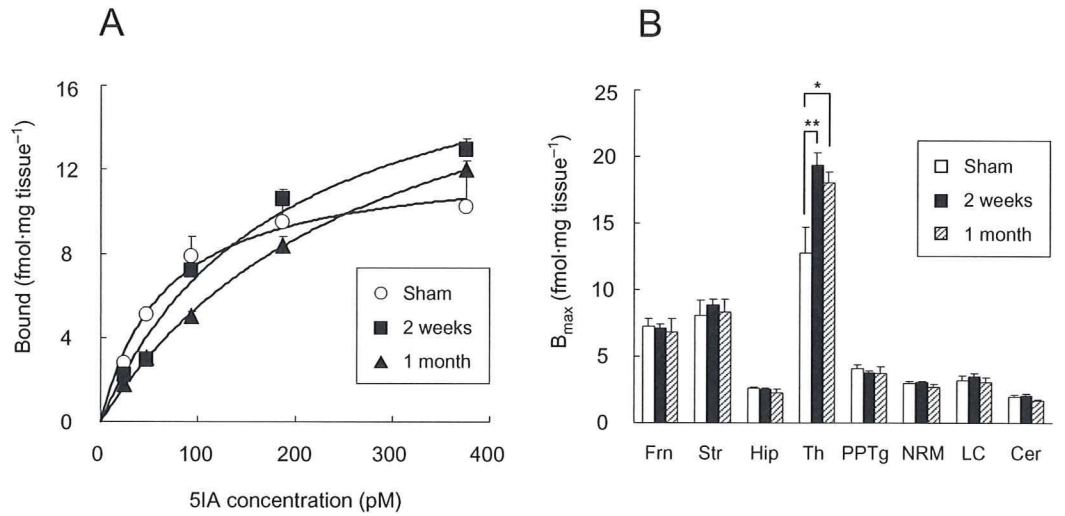

Figure 3 (A) Saturation curves of [^{125}I]5IA binding to sham-operated and PSL rat thalamus determined *ex vivo*. Each point represents the mean ± SEM of five to seven animals per group. The B_{max} values estimated by nonlinear regression analysis of these mean data were 12.5, 19.9 and 21.2 fmol/mg protein in sham-operated, 2 week post-PSL, and 1 month post-PSL group respectively. (B) Changes in nACh receptor density in brain regions of rats with Seltzer's PSL model of neuropathic pain. A significant increase was observed only in the thalamus, and no detectable change occurred in other regions. Each column represents the mean ± SEM of five to seven animals per group. *$P < 0.05$, **$P < 0.01$ versus sham. PSL, partial sciatic nerve ligation; 5IA, 5-iodo-3-(2(S)-azetidinylmethoxy)pyridine; Frn, frontal cortex; Str, striatum; Hip, hippocampus; Th, thalamus; PPTg, pedunculopontine tegmental nucleus; NRM, nucleus raphe magnus; LC, locus coeruleus; Cer, cerebellum.

presented in Figure 3A. As with the *ex vivo* autoradiography, both PSL groups showed a significant increase in B_{max} value that occurred in the thalamus only (Figure 3B). The percentage increase in B_{max} values in the thalamus (150%) was similar to those observed in the *ex vivo* autoradiographic findings.

Anti-allodynic effect of 5IA given intra-VPL

Based on previous reports (Kupers and Gybels, 1993; Derbyshire *et al.*, 1997; Gybels, 2001), we predicted that the VPL was involved in the expression of anti-nociceptive effects and investigated the association between nACh receptors expressed in the VPL and the anti-allodynic effect of 5IA.

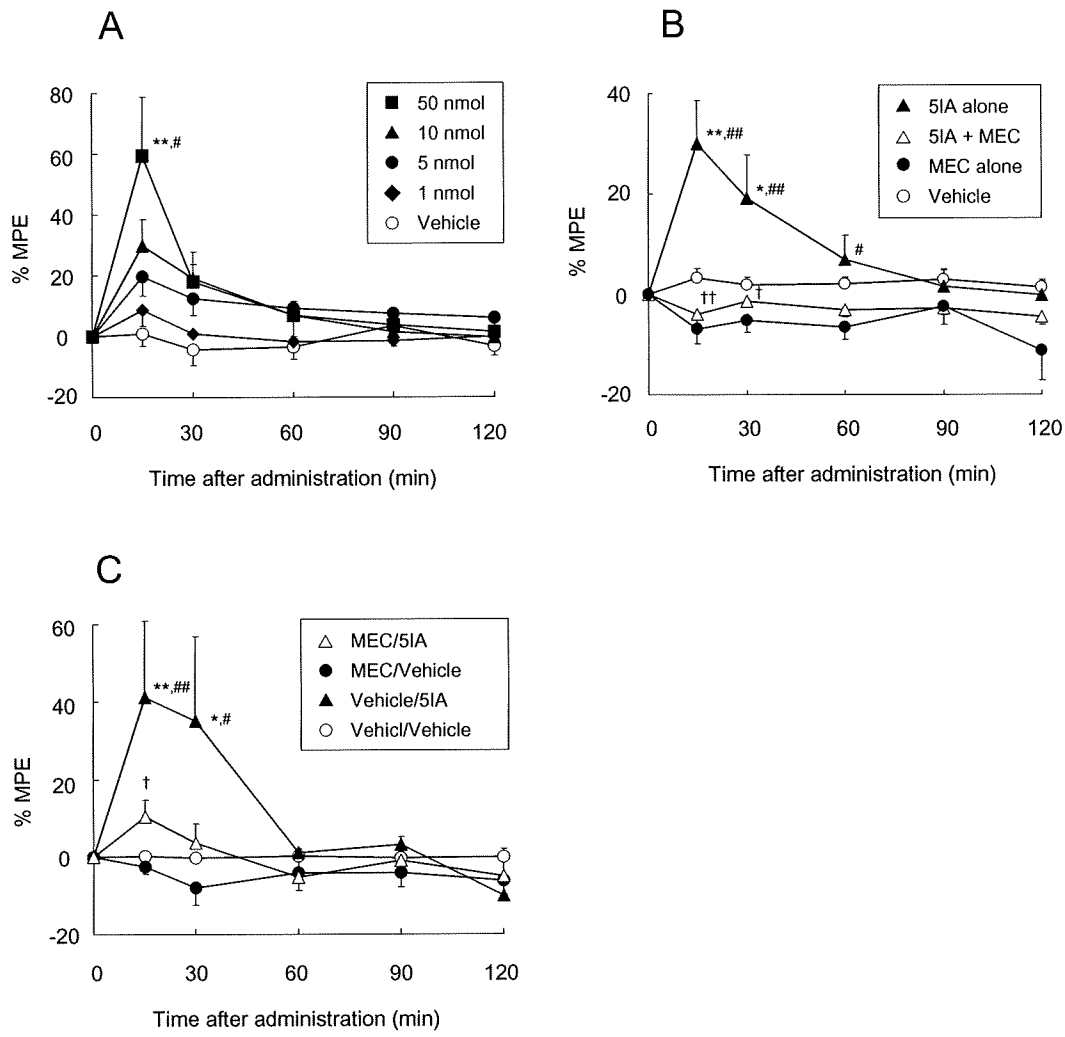

Figure 4 (A) Effect of 5IA injected intra-VPL on neuropathic tactile allodynia. Data are presented as a percentage of the maximum possible effect (% MPE). Each point represents the mean ± SEM of the ligated paws of five to six animals per group. $*P < 0.05$, $**P < 0.01$ versus vehicle, and $\#P < 0.05$ versus 1 nmol of 5IA at the same time point. (B) Effect of mecamylamine (MEC, 10 nmol in 0.5 μL) administered concurrently with 5IA in an intra-VPL manner on the anti-allodynic effect produced by 5IA (10 nmol in 0.5 μL, intra-VPL). Data are presented as a percentage of the maximum possible effect. Each point represents the mean ± SEM of the ligated paws of five to six animals per group. $*P < 0.05$, $**P < 0.01$ versus vehicle, $\#P < 0.05$, $\#\#P < 0.01$ versus MEC alone, and $\dagger P < 0.05$, $\dagger\dagger P < 0.01$ versus 5IA alone at the same time point. (C) Effect of mecamylamine (MEC, 10 nmol in 0.5 μL, intra-VPL, 5 min prior) on the anti-allodynic effect produced by 5IA (10 nmol in 5 μL, i.c.v.). Data are presented as a percentage of the maximum possible effect. Each point represents the mean ± SEM of the ligated paws of four to seven animals per group. $*P < 0.05$, $**P < 0.01$ versus vehicle/vehicle, $\#P < 0.05$, $\#\#P < 0.01$ versus MEC/vehicle, and $\dagger P < 0.05$ versus vehicle/5IA at the same time point. 5IA, 5-iodo-3-(2(S)-azetidinylmethoxy)pyridine; MPE, maximal possible effect; VPL, ventral posterolateral thalamic nucleus.

Figure 4A shows the anti-allodynic effects that occurred in the ligated paws of rats that received 5IA intra-VPL. Two-way ANOVA demonstrated significant main effects of treatment ($F_{4,115} = 3.97$, $P = 0.014$) and time ($F_{4,115} = 13.6$, $P < 0.001$) and a significant interaction between treatment and time ($F_{16,115} = 3.11$, $P < 0.001$). There was a significant difference between the 50 nmol-treated group and the vehicle- or 1 nmol-treated groups. Although one-way ANOVA revealed a significant difference between the data at 30 min after administration ($P = 0.028$), the *post hoc* Tukey test showed no significant difference.

Subsequently, we injected a mixed solution of 5IA and mecamylamine (10 nmol each) intra-VPL and performed the von Frey filament test. Two-way ANOVA demonstrated significant main effects of treatment ($F_{3,85} = 11.34$, $P < 0.001$) and time ($F_{4,85} = 5.22$, $P = 0.001$) and a significant interaction between treatment and time ($F_{12,85} = 4.05$, $P < 0.001$). Mecamylamine antagonized the 5IA-induced anti-allodynic effect completely, and furthermore, the % MPE values of mecamylamine-treated rats tended to decrease compared with those of the vehicle-treated rats, although the difference was not significant (Figure 4B).

Involvement of nACh receptors in the VPL in the anti-allodynic effect induced by i.c.v. 5IA administration

To explore to what extent nACh receptors in the VPL were involved in the anti-allodynic effects arising from central

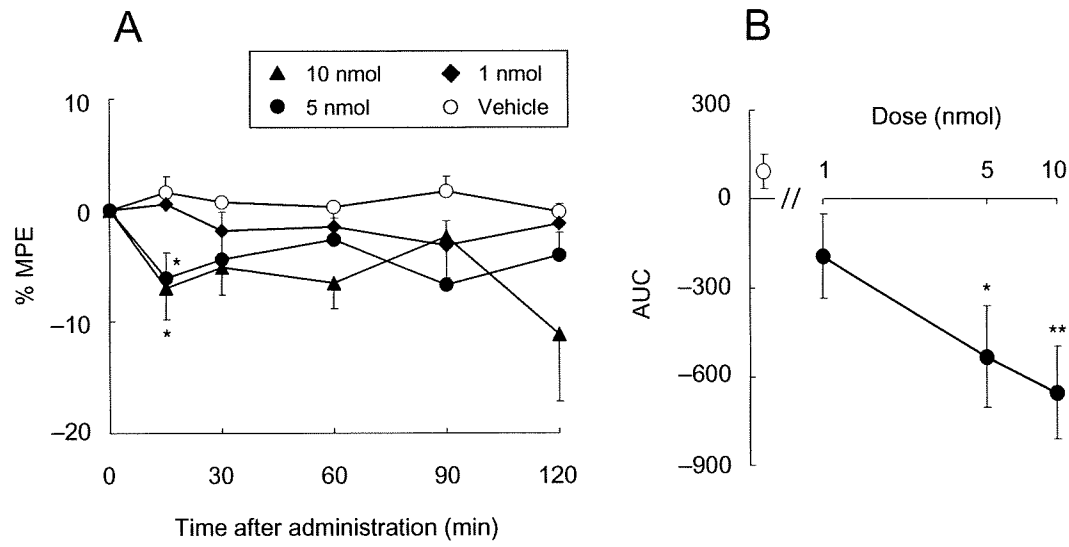

Figure 5 (A) Effect of mecamylamine injected intra-VPL on neuropathic tactile allodynia. Data are presented as a percentage of the maximum possible effect (% MPE). Each point represents the mean ± SEM of the ligated paws of five to six animals per group. $^{*}P < 0.05$ versus vehicle at the same time point. (B) Dose-response curve of mecamylamine-induced hyperalgesia. The open symbol represents the AUC of the vehicle-treated group, and the closed symbols represent that of each concentration of the mecamylamine-treated group. $^{*}P < 0.05$, $^{**}P < 0.01$ versus vehicle. AUC, area under the curves; MPE, maximal possible effect; VPL, ventral posterolateral thalamic nucleus.

nACh receptor activation, we evaluated the effect of intra-VPL administered mecamylamine on the anti-allodynic effects produced by i.c.v. administered 5IA. The results from the ligated paws are illustrated in Figure 4C. Two-way ANOVA demonstrated significant main effects of treatment ($F_{3,105} = 7.91$, $P = 0.001$) and time ($F_{4,105} = 5.65$, $P < 0.001$) and a significant interaction between treatment and time ($F_{12,105} = 2.49$, $P = 0.008$). The rats administered vehicle intra-VPL followed by 10 nmol of 5IA i.c.v. (Vehicle/5IA group) demonstrated significantly elevated % MPE values at 15 and 30 min after administration. This result was consistent with the anti-allodynic effect produced by i.c.v. administered 5IA (Figure 1). Pretreatment with intra-VPL mecamylamine (10 nmol) significantly inhibited the effect of i.c.v. administered 5IA (10 nmol). The % MPE values for rats treated with mecamylamine alone (MEC/Vehicle group) also tended to decrease compared with those of the vehicle treated rats, although the difference was not significant.

Hyperalgesic effect of intra-VPL administered mecamylamine

To examine the effects of mecamylamine on tactile allodynia in more detail, we injected multiple doses of mecamylamine intra-VPL and performed the von Frey filament test. Data from the ligated paws are shown in Figure 5A. There was a significant main effect of treatment ($F_{3,95} = 6.77$, $P = 0.003$) but no effect of time nor interaction between time and treatment. The *post hoc* Tukey test demonstrated a significant difference between vehicle-treated group and 5 nmol- or 10 nmol-treated groups. The calculated area under the curves of each group clearly demonstrated the dose-dependent hyperalgesic effects of mecamylamine (Figure 5B).

Effects of 5IA and mecamylamine on motor function

We conducted an inclined plane test to evaluate the effects of 5IA and mecamylamine on general motor functions. The maximum angle that the rats were able to endure before slipping down the plane was not significantly different between the vehicle and drug-treated groups at any time point (Table 1, data not shown for mecamylamine).

Table 1 Effects of 5IA on motor functions

Drug	*Time after administration*				
	15 min	*30 min*	*60 min*	*90 min*	*120 min*
i.c.v.					
Vehicle	98 ± 1	102 ± 4	98 ± 2	92 ± 3	94 ± 3
5IA	93 ± 2	97 ± 3	88 ± 4	96 ± 3	93 ± 1
Intra-VPL					
Vehicle	99 ± 3	99 ± 2	97 ± 4	100 ± 2	97 ± 3
5IA	100 ± 4	97 ± 2	99 ± 2	97 ± 1	102 ± 2

Data are expressed as a percentage of the control level ('angle of sliding'), which was determined before drug administration in each animal, and represent the mean ± SEM of five to six animals per group. No significant difference was observed between the two groups (two-way ANOVA with repeated measures).
5IA, 5-iodo-3-(2(S)-azetidinylmethoxy)pyridine; VPL, ventral posterolateral thalamic nucleus.

Discussion and Conclusions

In the present study, we examined the changes in central nACh receptor density in a rat model of neuropathic pain and the involvement of nACh receptors in anti-nociceptive effects in the region where changes occurred. First, we evaluated the anti-allodynic effect of 5IA after i.c.v. administration and found that the anti-allodynic effect was dose-dependent. Because the effect was completely antagonized by mecamylamine, the anti-allodynic effect of 5IA must occur via nACh receptors. No significant difference was observed between the

vehicle and 5IA treated groups in the inclined plane test suggesting that 5IA exhibited anti-allodynic effects without affecting motor functions.

We found that bilateral up-regulation of thalamic nACh receptors occurred in the PSL model of neuropathic pain. This is the first report of up-regulation of thalamic nACh receptors under chronic painful conditions. Because the up-regulation of both muscarinic and cannabinoid CB_1 receptors have been reported to contribute to the increased analgesic efficacy of each agonist (Siegling *et al.*, 2001; Chen and Pan, 2003), up-regulated nACh receptors may also contribute to the potentiation of anti-allodynic effects produced by nACh receptor agonists and attenuate neuropathic pain. Consistent with Seltzer's report (Seltzer *et al.*, 1990), the unilateral PSL caused bilateral tactile allodynia in the present study; and thus, the up-regulation must occur bilaterally. In the present study, we performed an autoradiographic saturation assay to determine the regional B_{max} of nACh receptors. As no report concerning autoradiographic saturation assays using [^{125}I]5IA has been published, it is important to validate the method used. Doura *et al.* (2008) performed quantitative autoradiography using [^{125}I]5IA, but, in their study, they incubated brain slices with only a single concentration of [^{125}I]5IA and did not perform a saturation assay. Thus, a direct comparison between our present data and theirs is not possible. Nevertheless, the ratios of the thalamus to the striatum or the cortex of our present data were consistent in the data reported by Doura *et al.* (2008), suggesting that our method was valid.

A previous PET study showed that the increase in cerebral blood flow in the VPL positively correlated with pain intensity, suggesting involvement of the VPL in pain transmission (Derbyshire *et al.*, 1997). Furthermore, electrical stimulation of the VPL has produced pain alleviation in both rat models and patients with neuropathic pain (Kupers and Gybels, 1993; Gybels, 2001). These findings suggest that the VPL is involved in the expression of anti-nociceptive effects. Indeed, we demonstrated that 5IA administered locally into the VPL significantly and dose-dependently reversed tactile allodynia. This effect was antagonized by coadministered mecamylamine. As no significant difference was observed between the vehicle and 5IA treated groups in the results of an inclined plane test, the changes in % MPE values observed in the 5IA treated groups were considered to reflect the analgesic effect, not motor dysfunction. These findings suggest that the nACh receptors expressed in the VPL were involved in the anti-allodynic effect that occurred after nACh receptor agonist administration. This was consistent with the finding that blockade of nACh receptors in the VPL caused a decrease in the anti-allodynic effect of i.c.v.-administered 5IA. Moreover, the intra-VPL injection of mecamylamine alone induced significant decreases in % MPE values. Mecamylamine is not an inverse agonist, but a non-competitive antagonist (Jensen *et al.*, 2005). Thus, during neuropathic pain, an intrinsic anti-allodynic mechanism by which ACh activates nACh receptors expressed in the VPL may be present and antagonism of these receptors by mecamylamine causes the hyperalgesic effect. That is to say, the nACh receptors expressed in the VPL may participate in anti-allodynic effects produced not only by exogenous but also endogenous agonists.

The present findings do not negate the involvement of nACh receptors in anti-allodynic effects outside of the VPL. Previous pharmacological studies reported that the central sites involved in nACh receptor-mediated antinociception were the NRM and the PPTg. The antinociception produced by nicotinic stimulation of the PPTg or the NRM depended upon muscarinic cholinergic, 5-hydroxytryptaminergic and adrenergic systems at the level of the lumbar spinal cord (Iwamoto and Marion, 1993). Curzon *et al.* (1998) showed that microinjection of nACh receptor agonists (epibatidine and A-85380) into the NRM produced antinociception against heat stimuli, and these effects were prevented by coadministration of mecamylamine into the NRM. Indeed, we demonstrated that VPL blockade by mecamylamine before i.c.v. administration of 5IA decreased the anti-allodynic effect by up to approximately 70%, not 100%. Thus, the remainder of the anti-allodynic effect is possibly caused by the binding of 5IA to the NRM and/or the PPTg.

Recently, Mogg *et al.* (2004) have reported that 5IA can functionally activate the α4β2-nACh and α6β2-nACh receptors. However, Perry *et al.* have reported that the nACh receptors expressed in the thalamus are mainly of the α4β2 sub-type (Perry *et al.*, 2002) and that the α6 subunit is present in less than 4% of the thalamic nACh receptors (Perry *et al.*, 2007). Therefore, the anti-allodynic effect we reported was probably mediated via the α4β2-nACh receptors, at least when 5IA was administered into the VPL. Whereas many results have shown that α4 subunit-containing nACh receptors play an important role in nACh receptor-mediated antinociception (Bitner *et al.*, 1998; Marubio *et al.*, 1999; Bitner *et al.*, 2000), the contribution of the α6β2-nACh receptors to the anti-nociceptive effect is unknown. As A-186253 has been developed as a specific antagonist of the α4β2-nACh receptors (Itier *et al.*, 2004), it may be possible to investigate α6β2-nACh receptor-mediated antinociception using both 5IA and A-186253.

In summary, we have demonstrated for the first time that up-regulation of thalamic nACh receptors occurs in a model of chronic pain. Moreover, we found that intra-VPL administration of 5IA attenuated tactile allodynia, dose-dependently. This effect was completely antagonized by co-administered mecamylamine. The blockade of nACh receptors in the VPL by mecamylamine caused a decrease in the anti-allodynic effect of i.c.v.-administered 5IA. These findings indicate that the nACh receptors expressed in the VPL are a potential site of the anti-nociceptive action produced by 5IA. Furthermore, mecamylamine, given intra-VPL, induced a hyperalgesic effect. This effect is likely to be responsible for the mecamylamine antagonism of the intrinsic anti-allodynic mechanism induced by endogenous acetylcholine. These findings suggest that the nACh receptors expressed in the VPL play an important role in the anti-allodynic effects produced by exogenous and endogenous agonists.

Acknowledgements

We thank Dr Takayuki Nakagawa (Department of Molecular Pharmacology, Graduate School of Pharmaceutical Sciences, Kyoto University) for his technical support and invaluable discussion regarding the behavioural tests. This work was

supported in part by a Grant-in-Aid for Scientific Research (A) (19209041) and a Grant-in-Aid for Young Scientists (B) (19790869) from the Ministry of Education, Culture, Sports, Science and Technology of Japan, and a grant from the Smoking Research Foundation.

Conflicts of interest

The authors state that they have no conflicts of interest.

References

Alexander SPH, Mathie A, Peters JA (2008). Guide to Receptors and Channels (GRAC), 3rd edn. *Br J Pharmacol* **153** (Suppl. 2): S1–S209.

Bannon AW, Decker MW, Curzon P, Buckley MJ, Kim DJ, Radek RJ *et al.* (1998a). ABT-594 [(R)-5-(2-azetidinylmethoxy)-2-chloropyridine]: a novel, orally effective antinociceptive agent acting via neuronal nicotinic acetylcholine receptors: II. In vivo characterization. *J Pharmacol Exp Ther* **285**: 787–794.

Bannon AW, Decker MW, Holladay MW, Curzon P, Donnelly-Roberts D, Puttfarcken PS *et al.* (1998b). Broad-spectrum, non-opioid analgesic activity by selective modulation of neuronal nicotinic acetylcholine receptors. *Science* **279**: 77–81.

Bannon AW, Decker MW, Kim DJ, Campbell JE, Arneric SP (1998c). ABT-594, a novel cholinergic channel modulator, is efficacious in nerve ligation and diabetic neuropathy models of neuropathic pain. *Brain Res* **801**: 158–163.

Bitner RS, Nikkel AL, Curzon P, Arneric SP, Bannon AW, Decker MW (1998). Role of the nucleus raphe magnus in antinociception produced by ABT-594: immediate early gene responses possibly linked to neuronal nicotinic acetylcholine receptors on serotonergic neurons. *J Neurosci* **18**: 5426–5432.

Bitner RS, Nikkel AL, Curzon P, Donnelly-Roberts DL, Puttfarcken PS, Namovic M *et al.* (2000). Reduced nicotinic receptor-mediated antinociception following in vivo antisense knock-down in rat. *Brain Res* **871**: 66–74.

Brasic JR, Zhou Y, Musachio JL, Hilton J, Fan H, Crabb A *et al.* (2009). Single photon emission computed tomography experience with (S)-5-[(123)I]iodo-3-(2-azetidinylmethoxy)pyridine in the living human brain of smokers and nonsmokers. *Synapse* **63**: 339–358.

Chen SR, Pan HL (2003). Up-regulation of spinal muscarinic receptors and increased antinociceptive effect of intrathecal muscarine in diabetic rats. *J Pharmacol Exp Ther* **307**: 676–681.

Curzon P, Nikkel AL, Bannon AW, Arneric SP, Decker MW (1998). Differences between the antinociceptive effects of the cholinergic channel activators A-85380 and (+/−)-epibatidine in rats. *J Pharmacol Exp Ther* **287**: 847–853.

Decker MW, Curzon P, Holladay MW, Nikkel AL, Bitner RS, Bannon AW *et al.* (1998). The role of neuronal nicotinic acetylcholine receptors in antinociception: effects of ABT-594. *J Physiol Paris* **92**: 221–224.

Decker MW, Rueter LE, Bitner RS (2004). Nicotinic acetylcholine receptor agonists: a potential new class of analgesics. *Curr Top Med Chem* **4**: 369–384.

Derbyshire SW, Jones AK, Gyulai F, Clark S, Townsend D, Firestone LL (1997). Pain processing during three levels of noxious stimulation produces differential patterns of central activity. *Pain* **73**: 431–445.

Donnelly-Roberts DL, Puttfarcken PS, Kuntzweiler TA, Briggs CA, Anderson DJ, Campbell JE *et al.* (1998). ABT-594 [(R)-5-(2-azetidinylmethoxy)-2-chloropyridine]: a novel, orally effective analgesic acting via neuronal nicotinic acetylcholine receptors: I. In vitro characterization. *J Pharmacol Exp Ther* **285**: 777–786.

Doura MB, Gold AB, Keller AB, Perry DC (2008). Adult and periadolescent rats differ in expression of nicotinic cholinergic receptor subtypes and in the response of these subtypes to chronic nicotine exposure. *Brain Res* **1215**: 40–52.

Fukui M, Nakagawa T, Minami M, Satoh M (2001). Antinociceptive effects of intracerebroventricularly administered P2 purinoceptor agonists in the rat. *Eur J Pharmacol* **419**: 25–31.

Gybels J (2001). Thalamic stimulation in neuropathic pain: 27 years later. *Acta Neurol Belg* **101**: 65–71.

Holladay MW, Wasicak JT, Lin NH, He Y, Ryther KB, Bannon AW *et al.* (1998). Identification and initial structure-activity relationships of (R)-5-(2-azetidinylmethoxy)-2-chloropyridine (ABT-594), a potent, orally active, non-opiate analgesic agent acting via neuronal nicotinic acetylcholine receptors. *J Med Chem* **41**: 407–412.

Itier V, Schonbachler R, Tribollet E, Honer M, Prinz K, Marguerat A *et al.* (2004). A-186253, a specific antagonist of the alpha 4 beta 2 nAChRs: its properties and potential to study brain nicotinic acetylcholine receptors. *Neuropharmacology* **47**: 538–557.

Iwamoto ET, Marion L (1993). Adrenergic, serotonergic and cholinergic components of nicotinic antinociception in rats. *J Pharmacol Exp Ther* **265**: 777–789.

Jain KK (2004). Modulators of nicotinic acetylcholine receptors as analgesics. *Curr Opin Investig Drugs* **5**: 76–81.

Jensen AA, Frolund B, Liljefors T, Krogsgaard-Larsen P (2005). Neuronal nicotinic acetylcholine receptors: structural revelations, target identifications, and therapeutic inspirations. *J Med Chem* **48**: 4705–4745.

Kanegawa N, Kiyono Y, Kimura H, Sugita T, Kajiyama S, Kawashima H *et al.* (2006). Synthesis and evaluation of radioiodinated (S,S)-2-(alpha-(2-iodophenoxy)benzyl)morpholine for imaging brain norepinephrine transporter. *Eur J Nucl Med Mol Imaging* **33**: 639–647.

Kupers RC, Gybels JM (1993). Electrical stimulation of the ventroposterolateral thalamic nucleus (VPL) reduces mechanical allodynia in a rat model of neuropathic pain. *Neurosci Lett* **150**: 95–98.

Mamede M, Ishizu K, Ueda M, Mukai T, Iida Y, Fukuyama H *et al.* (2004). Quantification of human nicotinic acetylcholine receptors with ^{123}I-5IA SPECT. *J Nucl Med* **45**: 1458–1470.

Mamede M, Ishizu K, Ueda M, Mukai T, Iida Y, Kawashima H *et al.* (2007). Temporal change in human nicotinic acetylcholine receptor after smoking cessation: 5IA SPECT study. *J Nucl Med* **48**: 1829–1835.

Marcil J, Walczak JS, Guindon J, Ngoc AH, Lu S, Beaulieu P (2006). Antinociceptive effects of tetrodotoxin (TTX) in rodents. *Br J Anaesth* **96**: 761–768.

Marubio LM, del Mar Arroyo-Jimenez M, Cordero-Erausquin M, Lena C, Le Novere N, de Kerchove d'Exaerde A *et al.* (1999). Reduced antinociception in mice lacking neuronal nicotinic receptor subunits. *Nature* **398**: 805–810.

Mogg AJ, Jones FA, Pullar IA, Sharples CG, Wonnacott S (2004). Functional responses and subunit composition of presynaptic nicotinic receptor subtypes explored using the novel agonist 5-iodo-A-85380. *Neuropharmacology* **47**: 848–859.

Mukhin AG, Gundisch D, Horti AG, Koren AO, Tamagnan G, Kimes AS *et al.* (2000). 5-Iodo-A-85380, an alpha4beta2 subtype-selective ligand for nicotinic acetylcholine receptors. *Mol Pharmacol* **57**: 642–669.

Oishi N, Hashikawa K, Yoshida H, Ishizu K, Ueda M, Kawashima H *et al.* (2007). Quantification of nicotinic acetylcholine receptors in Parkinson's disease with (123)I-5IA SPECT. *J Neurol Sci* **256**: 52–60.

Okada M, Nakagawa T, Minami M, Satoh M (2002). Analgesic effects of intrathecal administration of P2Y nucleotide receptor agonists UTP and UDP in normal and neuropathic pain model rats. *J Pharmacol Exp Ther* **303**: 66–73.

Paxinos G, Watson C (2005). *The Rat Brain in Stereotaxic Coordinates*, 5th edn. Elsevier Academic Press: San Diego, CA.

Perry DC, Xiao Y, Nguyen HN, Musachio JL, Davila-Garcia MI, Kellar KJ (2002). Measuring nicotinic receptors with characteristics of alpha4beta2, alpha3beta2 and alpha3beta4 subtypes in rat tissues by autoradiography. *J Neurochem* **82**: 468–481.

Perry DC, Mao D, Gold AB, McIntosh JM, Pezzullo JC, Kellar KJ (2007). Chronic nicotine differentially regulates alpha6- and beta3-containing nicotinic cholinergic receptors in rat brain. *J Pharmacol Exp Ther* **322**: 306–315.

Saji H, Ogawa M, Ueda M, Iida Y, Magata Y, Tominaga A *et al.* (2002). Evaluation of radioiodinated 5-iodo-3-(2(S)-azetidinylmethoxy) pyridine as a ligand for SPECT investigations of brain nicotinic acetylcholine receptors. *Ann Nucl Med* **16**: 189–200.

Seltzer Z, Dubner R, Shir Y (1990). A novel behavioral model of neuropathic pain disorders produced in rats by partial sciatic nerve injury. *Pain* **43**: 205–218.

Siegling A, Hofmann HA, Denzer D, Mauler F, De Vry J (2001). Cannabinoid CB(1) receptor upregulation in a rat model of chronic neuropathic pain. *Eur J Pharmacol* **415**: R5–R7.

Sindrup SH, Jensen TS (1999). Efficacy of pharmacological treatments of neuropathic pain: an update and effect related to mechanism of drug action. *Pain* **83**: 389–400.

Suzdak PD, Foged C, Andersen KE (1994). Quantitative autoradiographic characterization of the binding of [^{3}H]tiagabine (NNC 05-328) to the GABA uptake carrier. *Brain Res* **647**: 231–241.

Tanaka K, Fukuuchi Y, Gomi S, Takashima S, Mihara B, Shirai T *et al.* (1993). Reduction in second-messenger ligand binding sites after brain ischemia – autoradiographic Bmax and Kd determinations using digital image analysis. *Brain Res Bull* **32**: 49–56.

Ueda M, Iida Y, Kitamura Y, Kawashima H, Ogawa M, Magata Y *et al.* (2008). 5-Iodo-A-85380, a specific ligand for alpha4beta2 nicotinic acetylcholine receptors, prevents glutamate neurotoxicity in rat cortical cultured neurons. *Brain Res* **1199**: 46–52.

Ueda M, Iida Y, Mukai T, Mamede M, Ishizu K, Ogawa M *et al.* (2004). 5-[^{123}I]Iodo-A-85380: assessment of pharmacological safety, radiation dosimetry and SPECT imaging of brain nicotinic receptors in healthy human subjects. *Ann Nucl Med* **18**: 337–344.

Vaupel DB, Tella SR, Huso DL, Mukhin AG, Baum I, Wagner VO *et al.* (2003). Pharmacology, toxicology, and radiation dosimetry evaluation of [I-123]5-I-a-85380, a radioligand for in vivo imaging of cerebral neuronal nicotinic acetylcholine receptors in humans. *Drug Dev Res* **58**: 149–168.

Yasuda T, Miki S, Yoshinaga N, Senba E (2005). Effects of amitriptyline and gabapentin on bilateral hyperalgesia observed in an animal model of unilateral axotomy. *Pain* **115**: 161–170.

Imaging of HIF-1-Active Tumor Hypoxia Using a Protein Effectively Delivered to and Specifically Stabilized in HIF-1-Active Tumor Cells

Takashi Kudo[1], Masashi Ueda[1,2], Yuji Kuge[1], Takahiro Mukai[3], Shotaro Tanaka[4], Maki Masutani[1], Yasushi Kiyono[2,5], Shinae Kizaka-Kondoh[4], Masahiro Hiraoka[4], and Hideo Saji[1]

[1]Department of Patho-Functional Bioanalysis, Graduate School of Pharmaceutical Sciences, Kyoto University, Kyoto, Japan; [2]Radioisotopes Research Laboratory, Faculty of Medicine, Kyoto University Hospital, Kyoto University, Kyoto, Japan; [3]Department of Biomolecular Recognition Chemistry, Graduate School of Pharmaceutical Sciences, Kyushu University, Fukuoka, Japan; [4]Department of Radiation Oncology and Image-Applied Therapy, Kyoto University Graduate School of Medicine, Kyoto University, Kyoto, Japan; and [5]Biomedical Imaging Research Center, University of Fukui, Fukui, Japan

Hypoxia-inducible factor-1 (HIF-1) plays an important role in malignant tumor progression and in the development of resistance to radiotherapy. We designed a novel fusion protein (PTD-ODD-SAV [POS]) consisting of a protein transduction domain (PTD), streptavidin (SAV), and a portion of the oxygen-dependent degradation domain (ODD) of HIF-1α that confers the same oxygen-dependent regulation as HIF-1α on POS. (3-$^{123/125}$I-iodobenzoyl)norbiotinamide ($^{123/125}$I-IBB) was conjugated to the SAV moiety of POS to synthesize $^{123/125}$I-IBB-labeled POS ($^{123/125}$I-IPOS). The purpose of this study was to evaluate the feasibility of ^{123}I-IPOS as an imaging probe for HIF-1-active tumor hypoxia. **Methods:** After a 24-h incubation of ^{125}I-IPOS with various tumor cell lines under either normoxic (20% O_2) or hypoxic (0.1% O_2) conditions, the intracellular radioactivity was investigated. Then, the biodistribution of $^{123/125}$I-IPOS was examined with tumor-implanted mice, and an in vivo imaging study was performed. The tumoral accumulation of ^{125}I-IPOS was compared with HIF-1 activity using the mice carrying tumors with the HIF-1-dependent luciferase reporter gene. Furthermore, the intratumoral localization of ^{125}I-IPOS was examined by the autoradiographic study, and then the same slide was subjected to immunostaining for pimonidazole, which is the hypoxic marker. **Results:** The ratios of radioactivity in hypoxic cells to that in normoxic cells were more than 2. These results indicate incorporation of ^{125}I-IPOS into these cells and degradation of ^{125}I-IPOS by normoxic tumor cells. In the biodistribution study, ^{125}I-IPOS accumulated in the tumor (1.4 ± 0.3 percentage injected dose per gram) 24 h after administration. At that time, ^{125}I-IPOS showed high tumor-to-blood and tumor-to-muscle ratios (5.1 ± 0.3 and 14.0 ± 3.9, respectively). The tumors were clearly visualized by in vivo imaging 24 h after ^{123}I-IPOS injection (tumor-to-muscle ratio was 9.6). The tumoral accumulation of ^{125}I-IPOS correlated with HIF-1 activity ($R = 0.71$, $P < 0.05$), and its intratumoral distribution coincided with the hypoxic regions. **Conclusion:** ^{123}I-IPOS is a potential probe for the imaging of HIF-1 activity in tumors. Given the role of HIF-1 in tumor biology, its detection may be considered an indicator of aggressive cancer phenotypes.

Key Words: molecular imaging; oncology; radiopharmaceuticals; hypoxia-inducible factor-1 (HIF-1); tumor hypoxia; oxygen-dependent degradation (ODD); protein transduction domain (PTD)

J Nucl Med 2009; 50:942–949
DOI: 10.2967/jnumed.108.061119

In solid tumors, hypoxia, or an oxygen tension below physiologic levels, develops as abnormal proliferation outstrips the blood supply (*1*). This hypoxic region is involved in tumor malignancy and proliferation and results in the development of resistance to radiotherapy (*2–4*). Hypoxia-inducible factor-1 (HIF-1), a transcription factor that regulates the cellular response to hypoxia, induces several genes that mediate these changes in tumor behavior (*5,6*). Indeed, HIF-1-active or hypoxic cells have recently been shown to play crucial roles in angiogenesis and radioresistance (*7*). Finally, the expression level of HIF-1 correlates with a poor prognosis in many tumors (*8,9*). Thus, imaging HIF-1-active regions in a tumor has the potential to provide, in a noninvasive manner, insight into those aspects of tumor biology most relevant to treatment design.

HIF-1 is a heterodimer that consists of the oxygen-sensitive α-subunit (HIF-1α) and the constitutively expressed β-subunit (HIF-1β). Under normoxic conditions, HIF-1α is hydroxylated by prolyl hydroxylases on the proline residues in the oxygen-dependent degradation domain (ODD). The hydroxylated proline residues accelerate ubiquitination of ODD

Received Dec. 14, 2008; revision accepted Feb. 16, 2009.
For correspondence or reprints contact: Hideo Saji, Department of Patho-Functional Bioanalysis, Graduate School of Pharmaceutical Sciences, Kyoto University, 46-29 Yoshida-Shimo-Adachi-cho, Sakyo-ku, Kyoto 606-8501, Japan.
E-mail: hsaji@pharm.kyoto-u.ac.jp

and subsequent degradation of HIF-1α (*10*). HIF-1α expression is regulated in an oxygen-dependent manner at the posttranscriptional level and is responsible for regulation of HIF-1 activity (*11*).

We recently developed TOP3 (TAT-ODD-procaspase-3), a fusion protein with 3 domains: TAT-PTD, ODD, and procaspase-3 (*12–16*). The protein transduction domain (PTD) is derived from the PTD of the HIV type 1 TAT protein (*17*) and efficiently delivers TOP3 to any tissue in vivo. The ODD domain contains a von Hippel Lindau–mediated protein destruction motif of human HIF-1α protein (*18*) and confers hypoxia-dependent stabilization on TOP3 (*14*). Intraperitoneal injection of TOP3 into tumor-bearing mice results in specific targeting of HIF-1-active tumor cells (*7,12*). These results demonstrated that PTD-ODD fusion proteins were efficiently delivered to hypoxic regions and stabilized in HIF-1-active cells.

In this study, we took advantage of the PTD-ODD fusion proteins for imaging of HIF-1-active hypoxic tumors. To label PTD-ODD with a radioactive reagent, PTD3-ODD was fused to a monomeric streptavidin (SAV). The SAV component was then used to join the compound to a radiolabeled biotin derivative, (3-^{123}I-iodobenzoyl)norbiotinamide (^{123}I-IBB). Our concept of hypoxia imaging is summarized in Figure 1. In this study, we evaluated the feasibility of ^{123}I-IBB-labeled PTD-ODD-SAV (^{123}I-IPOS) as an imaging probe for HIF-1-active tumor hypoxia.

MATERIALS AND METHODS

Construction of Plasmid and Preparation of Recombinant Protein POS

To construct the pGEX/POS plasmid encoding the POS fusion protein, the cDNAs encoding PTD3 and $ODD_{548–603}$ were constructed as described previously (*18,19*). The cDNA encoding the spacer sequence VDVADLEHD was constructed by annealing synthesized oligonucleotides corresponding to the polypeptide to *Bgl*II and *Bam*HI endonuclease restriction sites at the 5′ and 3′ sites, respectively. SAV cDNA was amplified by polymerase chain reaction using corresponding oligonucleotides as primers and a bacterial genome as a template. The resultant cDNA encoded the SAV protein from its 25th amino acid to the C terminus and had *Kpn*I and *Xho*I endonuclease restriction sites at the 5′ and 3′ sites, respectively. The cDNA encoding POS was constructed by ligating the cDNAs constructed above into the *Eco*RI and *Xho*I sites of the pGEX-6P-3 vector (GE Healthcare Bioscience). The resultant pGEX/POS vector encoded GST-tagged POS and was transformed into BL21(DE3)plysS (Novagen). GST-POS recombinant protein was induced with 1 mM isopropyl-β-d-thiogalactopyranoside for 24 h at 4°C and purified over a glutathatione Sepharose 4B column (GE Healthcare Bioscience). The GST-tag was removed from the recombinant protein with PreScission Protease (GE Healthcare Bioscience) in the column. The eluate containing POS was then dialyzed against 10 mM Tris-hydrochloric acid buffer (pH 8.0) and concentrated using the Amicon Ultra-15 5k NMWL device (Millipore). The purity and molecular weight of POS were determined by sodium dodecylsulfate-polyacrylamide gel electrophoresis and Coomassie staining.

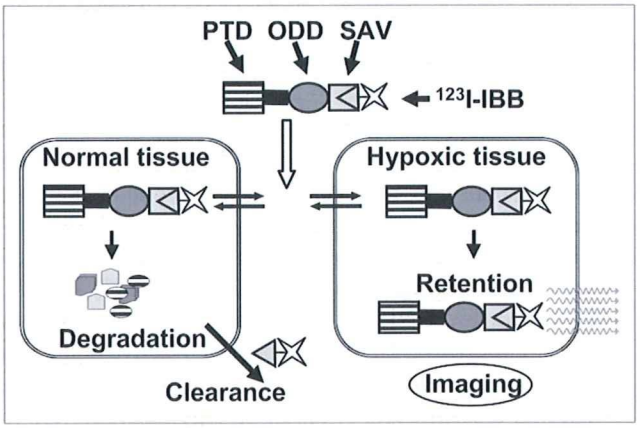

FIGURE 1. Concept of hypoxia imaging using ^{123}I-IPOS. PTD enables ^{123}I-IPOS to be delivered to normoxic and hypoxic tissue. In normoxic tissue, POS is degraded in manner similar to HIF-1α degradation, and ^{123}I-IBB is cleared. In contrast, in HIF-1-active tissues, POS escapes degradation and radioactivity is retained within cell. Thus, POS enables specific imaging of HIF-1-active hypoxic region.

Synthesis of IBB

IBB was prepared as previously described (*20*). The products were obtained as white crystals and stored under argon at 4°C (yield, 30.5%).

Radiosynthesis of ^{123}I-IBB and ^{125}I-IBB

Ammonium ^{123}I-iodide was kindly provided by Nihon Medi-Physics. Sodium ^{125}I-iodide was purchased from Perkin Elmer Life and Analytic Sciences. All other chemicals used were of reagent grade. A total of 1 GBq $NH_4{}^{123}I$ or 37 MBq $Na^{125}I$ were added to a vial containing *N*-succinimidyl 3-(tributhylstannyl)benzoate (72.2 μL, 2 mg/mL of 1% acetic acid methanol) and *N*-chlorosuccinimide (19.8 μL, 0.5 mg/mL of methanol). The vial was vortexed and the reaction allowed to proceed at room temperature for 30 min. $NaHSO_3$ (3.2 μL, 0.72 mg/mL in H_2O) was added to the product, which was vortexed before being concentrated under a stream of nitrogen. A solution of norbioinamine·hydrochloric acid in dimethylformamide:water (4:1) (100 μL, 3 mg/mL) was added to the vial. The reaction was incubated at room temperature for 2 h, and the sample was purified with high-performance liquid chromatography (HPLC) (Cosmosil $5C_{18}$-AR-300 column, 4.6 mm × 15 cm; Nacalai Tesque) (25% acetonitrile, 1 mL/min; wave length, 254 nm). The retention time of IBB was 21 min. The solvent was evaporated and was reconstituted in water for use in the in vitro and in vivo studies. The radiochemical purity was confirmed with HPLC using the same method as was used for purification.

Cell Culture

MM1, HeLa, and Suit2 cells were obtained from American Type Culture Collection. FM3A cells were purchased from the Health Science Research Resources Bank, and MDA-MB-231 cells were purchased from Dainippon Sumitomo Pharma Co., Ltd. MM1, HeLa, and Suit2/HRE-luciferase (*19*) cells were maintained in 10% fetal bovine serum–Dulbecco's modified Eagle's medium (Nissui Pharmaceutical). FM3A and MDA-MB-231 cells were cultured in 10% fetal bovine serum–RPMI medium (Nissui Pharmaceutical). The culture media were supplemented with penicillin (100 units/mL) and streptomycin (100 μg/mL). Cells were incubated at 37°C in

a well-humidified incubator with 5% CO_2 and 95% air for normoxic culture or incubated in an anaerobic chamber (Concept Mini MACS; Biotrace Limited) for hypoxic culture.

Binding of ^{125}I-IBB to POS

To prepare ^{125}I-IPOS, ^{125}I-IBB was added to a microtube containing POS (100 μL, 13.6 ng/mL). After a 1-h incubation, the reactant was purified by size-exclusion HPLC (TSKgel SuperSW2000 [4.6 mm × 30 cm] connected by the TSKguardcolumn SuperSW [4.6 mm × 3.5 cm]; Tosoh Corp.) (100 mM phosphate buffer [pH 6.8], 0.2 mL/min; wave length, 254 nm). The radiochemical purity was examined by paper chromatography developed with saline (R_f = 0).

Biotin Competitive Assay

^{125}I-IBB, D-biotin (0–40 pmol), and 100 mM citrate buffer (pH 5.0) were added to a microtube containing POS (1.36 ng). The reaction was performed at 37°C for 1 h. The reaction mixture was applied to an Amicon Microcon filter (Millipore) and centrifuged at 4°C and 4,500*g* for 30 min (Micro Cooling Centrifuge 1720; KUBOTA). The radioactivities of the reactant and filtrate were then measured and the binding rate calculated.

Cellular Assay

HeLa, MM1, and FM3A cells were transfected with the pGL3/5HRE-CMV_{mp}-luciferase plasmid, which induced luciferase expression in response to HIF-1 activity (*12*). Transfection was performed using reagent (Lipofectamin 2000; Invitrogen). After a 24-h incubation under normoxic (20% O_2) or hypoxic (0.1% O_2) conditions, cells were washed and lysed with Reporter Lysis Buffer (Promega), and luciferase activity was evaluated with a single tube luminometer (Lumat LB 9507; Berthold) using a Luciferase Assay System (Promega). The protein concentration was measured with the BCA Protein Assay Kit (Pierce) for normalization.

ODD-dependent, normoxic, POS degradation was evaluated by 2 assays. In the first assay, MM1, HeLa, and FM3A cells were incubated in advance for more than 6 h under either normoxic or hypoxic conditions, after which ^{125}I-IPOS (0.28 μg, 37 kBq) was added. Cells were then incubated for an additional 24 h in their respective culture conditions. After the cells were washed and lysed, the radioactivity of the lysate was measured using an auto well γ-counter (ARC2000; Aloka), and the protein concentration was measured and used for normalization. In the second assay, HeLa cells were incubated in advance for more than 6 h under hypoxic conditions, after which ^{125}I-IPOS (0.28 μg, 37 kBq) was added. The cells were then incubated for an additional 24 h under hypoxic conditions. After washing, the medium was replaced with fresh medium, and the cells were subjected to further incubation for 3 or 24 h under normoxic or hypoxic conditions. After the incubation, cells were washed and lysed, and the radioactivity and protein concentration of the lysate were measured. The radioactivities of the cells and medium were analyzed by ultrafiltration (Amicon Microcon filter; Millipore) and size-exclusion HPLC. All measurements were performed in triplicate.

Animal Model

Animal studies were conducted in accordance with our institutional guidelines, and the experimental procedures were approved by the Kyoto University Animal Care Committee. To produce the mouse models of tumor implantation, 5×10^6 FM3A cells in 100 μL of phosphate-buffered saline (PBS) were subcutaneously implanted into the right thighs of 5-wk-old female C3H/He mice (Japan SLC, Inc.). A total of 1×10^7 MDA-MB-231 cells or 5×10^6 Suit2/HRE-luciferase cells in 100 μL of PBS were subcutaneously implanted into the right thighs of 5-wk-old female BALB/c *nu/nu* mice (Japan SLC, Inc.). After the cells implanted, the mice were maintained on the AIN76-A–based biotin-free diet (Japan SLC, Inc.). FM3A and Suit2 tumor models were used 2 wk after implantation, and the MDA-MB-231 tumor models were used 1 mo after implantation for the tracer study.

Biodistribution

^{125}I-IPOS (0.05–30 μg, 37 kBq/mouse) or ^{125}I-IBB (37 kBq/mouse) was injected intravenously into FM3A-implanted mice. At the appropriate time points after administration, the mice were sacrificed. Whole-organ specimens were immediately removed and weighed, and the radioactivity was measured. The results were expressed as the percentage injected dose per gram (%ID/g).

In Vivo Imaging

^{123}I-IPOS (30 μg, 5.4–16 MBq) was injected in FM3A-implanted mice via the tail vein. The mice were anesthetized with 2.5% halothane and placed on the scanner bed in the prone position. Planar images were obtained for 10 min at 24 and 48 h after injection as previously described (*21*). Regions of interest were set on the tumor in the right thigh and the corresponding area in the left thigh.

Tumoral Accumulation of ^{125}I-IPOS Versus HIF-1 Transcriptional Activity in Vivo

The Suit2/HRE-luciferase–implanted mice were intravenously injected with ^{125}I-IPOS (30 μg, 37 kBq/mouse). After 24 h, 200 μL of D-luciferin solution (10 mg/mL in PBS; Promega) was injected intraperitoneally. After 20 min, the mice were anesthetized with 2.5% isoflurane and imaged using the IVIS Spectrum System (Xenogen) to measure the luciferase activity as the externally detected photon count. The photon counts within the tumors were analyzed with software (Living Image 3.0; Xenogen). After luciferase imaging, the mice were sacrificed and the tumors immediately removed. The radioactivity was then measured and the results expressed as the percentage injected dose (%ID).

Autoradiography

Autoradiographic studies of ^{125}I-IPOS were performed in MDA-MB-231–implanted mice. ^{125}I-IPOS (30 μg, 2.5 MBq/mouse) was injected intravenously, and at 22 h after injection pimonidazole (60 mg/kg) was injected intraperitoneally. Mice were sacrificed 2 h later. Autoradiograms were obtained as previously described (*21*), with the following slight modification: BAS5000 instead of BAS3000.

Immunohistochemistry

The slides used in the autoradiographic study were subjected to immunostaining for pimonidazole. The immunostaining was performed using the Hypoxyprobe-1 Plus Kit (Chemicon), according to the manufacturer's protocol. To evaluate the specificity of the signal, tumor sections derived from pimonidazole-untreated mice were also stained by following the same protocol.

Statistical Analyses

Comparisons between 2 groups were performed with the Mann–Whitney *U* test. Correlation coefficients were assessed using the Spearman rank analysis. A *P* value of less than 0.05 was considered statistically significant.

RESULTS

Construction of the Fusion Protein POS

The recombinant protein POS consisted of 3 parts: PTD, ODD, and SAV (Fig. 1). The PTD was composed of polylysine and hydrophobic amino acids, and was named PTD3. The ODD was $ODD_{548–603}$, the same as the one previously described in TOP3 (*7*). The spacer sequence VDVADLEHD was inserted between PTD and ODD for stabilization of the fusion protein. The molecular weight of the fusion protein was approximately 34 kDa (Fig. 2).

Radiosynthesis of ^{125}I-IBB and ^{123}I-IBB

^{125}I-IBB and ^{123}I-IBB were obtained in the absence of a carrier and with radiochemical yields of 65% and 29% and radiochemical purities of greater than 94% and greater than 95%, respectively (Supplemental Fig. 1; supplemental materials are available online only at http://jnm.snmjournals.org).

Binding of ^{125}I-IBB to POS

After the incubation of ^{125}I-IBB with POS, the radioactivity was detected at about 34 kDa by size-exclusion HPLC analysis, indicating that ^{125}I-IBB bound to POS to form ^{125}I-IPOS (Fig. 3A). This binding was inhibited by D-biotin in a dose-dependent manner (Fig. 3B).

Oxygen-Dependent Regulation of ^{125}I-IPOS In Vitro

To validate the stabilization of HIF-1α in our experimental conditions, we performed a luciferase assay using an HRE-responsive reporter system (*12*). The luciferase activities in HeLa, MM1, and FM3A cells, incubated under hypoxic conditions, were 28-, 17- and 29-fold higher than those of cells incubated under normoxic conditions, respectively (Fig. 4A).

We then added ^{125}I-IPOS to the culture medium of HeLa, MM1, and FM3A cells and compared the radioactivity retained in the cells after incubation under normoxic conditions with that after incubation under hypoxic conditions for 24 h. The ratios of the radioactivity in hypoxic cells to that in normoxic cells were 2.7, 2.2, and 2.3 in HeLa, MM1, and FM3A cells, respectively (Fig. 4B). Furthermore, the accumulated radioactivity under hypoxic conditions was decreased in a time-dependent manner after reoxygenation. After 24-h reoxygenation, the ratio of the radioactivity in hypoxic cells to that in reoxygenated cells was 1.8 ± 0.3 (Fig. 4C). The size-exclusion HPLC analysis revealed that more than 80% of the intracellular radioactivity was derived from intact ^{125}I-IPOS, and that approximately 70% of radioactivity in the reoxygenated medium was derived from ^{125}I-IBB and other small molecules (data not shown).

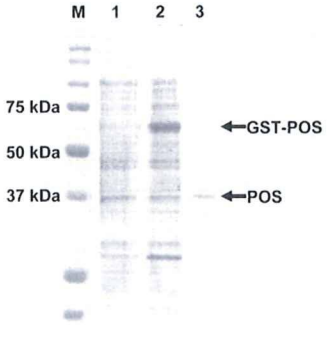

FIGURE 2. Analysis of fusion protein expression with sodium dodecylsulfate-polyacrylamide gel electrophoresis (lane M, molecular weight marker; lane 1, *Escherichia coli* lysate before IPTG induction; lane 2, *E. coli* lysate after IPTG induction; lane 3, protein solution after purification). New band was expressed in lane 2 at about 60 kDa, corresponding to GST-fused POS. After purification, only 1 band was detected in lane 3 at 34 kDa. IPTG = isopropyl-β-d-thiogalactopyranoside.

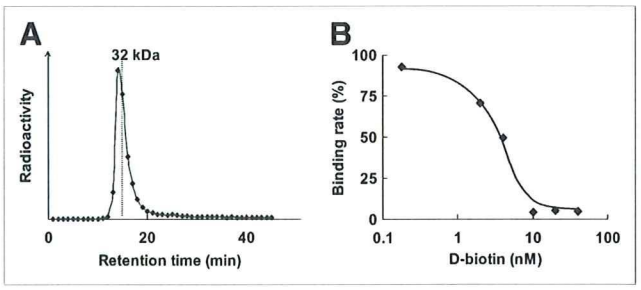

FIGURE 3. Binding of ^{125}I-IBB to POS. (A) Size-exclusion HPLC chromatogram after incubation of ^{125}I-IBB with POS. Symbols represent radioactivity of each eluate collected every 1 min. (B) Concentration-dependent inhibition of ^{125}I-IBB binding to POS by D-biotin. Symbols and bars represent mean and SD.

Biodistribution

When we examined the biodistribution of ^{125}I-IBB alone, the tumor-to-blood ratio was always less than 1 at each time point, indicating no tumor accumulation of ^{125}I-IBB (data not shown). Next, we performed a biodistribution study of ^{125}I-IPOS. A high level of radioactivity accumulated in the liver and the spleen, and a moderate level was present in the intestine and the kidneys. Though the radioactivity in the blood at 1 h after injection was higher than the corresponding data for ^{125}I-IBB (*20*), blood clearance was rapid. In contrast, the radioactivity tended to be retained in the tumor (1.47 %ID/g at 1 h and 1.49 %ID/g at 6 h). The tumor-to-blood ratio was greater than 1 at 24 h or more after injection (Table 1). We then evaluated whether the accumulation of ^{125}I-IPOS in the tumor was dose-dependent. There were no differences in the tumor accumulation and the tumor-to-blood ratio between the 0.05- and the 0.5-μg injected groups. However, a dose-dependent increase was observed when more than 0.5 μg of ^{125}I-IPOS was injected. The tumor accumulation and tumor–to–normal tissue ratio were highest in the 30-μg injected group (Table 2). The tumor accumulation was 1.4 %ID/g, the tumor-to-blood ratio was 5.1, and the tumor-to-muscle ratio was 14.0 at 24 h after injection (Table 2). Evaluation 48 h after injection demonstrated further increases in the tumor-to-blood ratio and the tumor-to-muscle ratio (12.8 and 22.3, respectively; data not shown).

In Vivo Imaging

The tumor was clearly visualized both at 24 and at 48 h after ^{123}I-IPOS injection (Fig. 5). At 24 and 48 h after

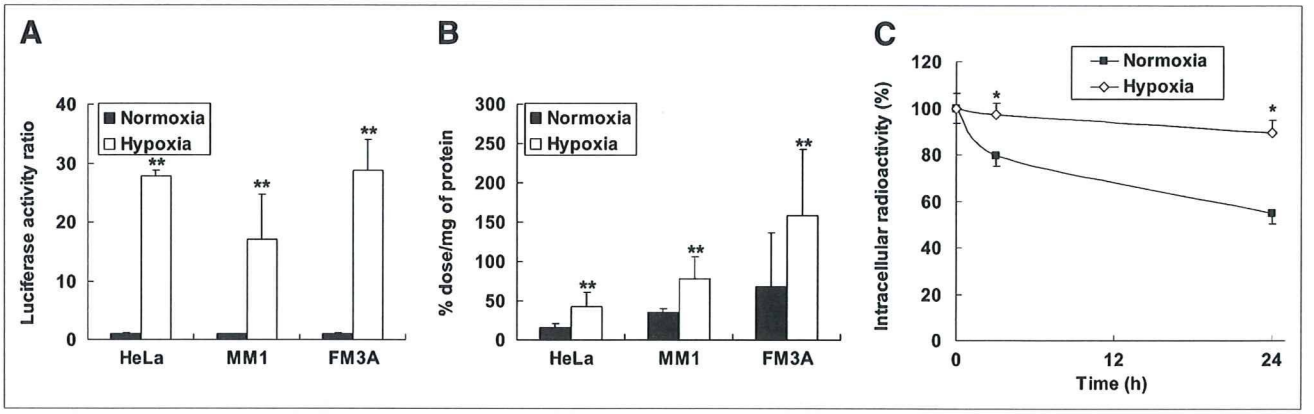

FIGURE 4. (A) HIF-1-dependent luciferase activity in HeLa, MM1, and FM3A cells. Data were normalized by protein concentration of cells. Results are shown as ratio of activity after hypoxia to activity after normoxia. Columns and bars represent mean and SD (n = 3–6 $^{**}P < 0.01$ vs. normoxia). (B) Intracellular radioactivity in HeLa, MM1, and FM3A cells after 24-h incubation under either normoxic or hypoxic conditions. Radioactivity was normalized by protein concentration of cells. Columns and bars represent mean and SD (n = 3–6 $^{**}P < 0.01$ vs. normoxia). (C) Degradation of intracellularly accumulated IPOS after reoxygenation. HeLa cells were incubated with ^{125}I-IPOS for 24 h under hypoxic conditions. Then, medium was replaced with fresh medium, and cells were subjected to further incubation under normoxic or hypoxic conditions. Results are shown as percentage of radioactivity at start of second incubation. Symbols and bars represent mean and SD (n = 3–5; $^{*}P < 0.05$ vs. normoxia).

injection, the calculated tumor-to-muscle ratios were 9.6 ± 4.7 and 20 ± 21, respectively (n = 6). Although the accumulation of ^{123}I-IPOS in the abdominal region was high, there was little accumulation in the thoracic region.

Comparison Between Tumoral Accumulation of ^{125}I-IPOS and HIF-1 Activity In Vivo

Figure 6 shows the highly significant correlation between luciferase activity and radioactivity (R = 0.71, $P < 0.05$).

Regional Distribution of ^{125}I-IPOS Relative to Hypoxic Regions in Tumor

Pimonidazole immunohistochemistry demonstrated hypoxic areas within the tumor (Fig. 7B). On the other hand, the section derived from pimonidazole-untreated mice was not stained (Fig. 7D). The autoradiogram represents the distribution of ^{125}I-IPOS in the tumor and shows that the distribution is heterogeneous and for the most part corresponds to the pimonidazole-positive hypoxic areas. However, there were also a few pimonidazole-positive regions that did not show accumulation of ^{125}I-IPOS (Figs. 7A and 7C).

DISCUSSION

HIF-1, which is activated by hypoxia, is associated with an aggressive cancer phenotype. Tumors expressing HIF-1 are resistant to radiation therapy and chemotherapy and as a result carry a poor prognosis. Noninvasive imaging of HIF-1 activity is of great interest because it may be used to predict prognosis. In our present study, we found that POS entered into tumor cells and was degraded in an oxygen-dependent manner, $^{123/125}$I-IPOS accumulated in tumors and the tumors were clearly visualized by in vivo imaging, the tumoral accumulation of ^{125}I-IPOS correlated with tumoral HIF-1

TABLE 1. Biodistribution of ^{125}I-IPOS in FM3A-Implanted Mice

	Time after injection (h)			
Organ	1	6	24	48
Blood	15.55 ± 1.06	3.14 ± 0.54	0.18 ± 0.12	0.01 ± 0.01
Liver	32.97 ± 1.03	13.80 ± 0.87	0.97 ± 0.44	0.30 ± 0.06
Spleen	17.29 ± 2.35	6.07 ± 0.73	1.21 ± 0.53	0.19 ± 0.05
Kidney	5.51 ± 0.36	2.79 ± 0.47	0.74 ± 0.60	0.09 ± 0.02
Stomach	2.25 ± 0.57	0.62 ± 0.32	0.49 ± 0.31	0.04 ± 0.02
Neck	2.39 ± 0.06	0.80 ± 0.08	0.09 ± 0.04	0.00 ± 0.01
Intestine	7.96 ± 0.09	9.82 ± 1.61	0.91 ± 0.13	0.24 ± 0.08
Tumor	1.47 ± 1.02	1.49 ± 0.38	0.28 ± 0.08	0.07 ± 0.05
Muscle	0.94 ± 0.65	0.28 ± 0.05	0.07 ± 0.06	0.00 ± 0.01
Tumor/blood	0.10 ± 0.07	0.49 ± 0.18	1.79 ± 0.59	6.72 ± 6.61

Organ uptake values are expressed as %ID/g of tissue except for tumor/blood. Values are mean ± SD; n = 3–5.

TABLE 2. Effect of POS Concentration on Biodistribution of ^{125}I-IPOS in FM3A-Implanted Mice at 24 Hours After Injection

Organ	Protein concentration (μg)			
	0.05	0.5	5	30
Blood	0.12 ± 0.04	0.16 ± 0.10	0.16 ± 0.01	0.27 ± 0.07
Liver	1.92 ± 0.24	1.27 ± 0.53	5.53 ± 1.05	13.61 ± 1.90
Spleen	1.07 ± 0.30	1.15 ± 0.41	2.33 ± 0.25	7.87 ± 2.20
Kidney	0.35 ± 0.20	0.59 ± 0.51	1.03 ± 0.10	4.32 ± 1.87
Stomach	0.28 ± 0.14	0.55 ± 0.42	0.52 ± 0.20	0.86 ± 0.27
Neck	0.05 ± 0.04	0.09 ± 0.04	0.11 ± 0.02	0.23 ± 0.08
Intestine	4.57 ± 0.82	1.95 ± 2.03	2.17 ± 0.24	2.18 ± 0.28
Tumor	0.23 ± 0.08	0.25 ± 0.07	0.49 ± 0.09	1.37 ± 0.33
Muscle	0.05 ± 0.03	0.05 ± 0.05	0.07 ± 0.01	0.10 ± 0.03
Tumor/blood	2.04 ± 0.61	1.61 ± 0.10	3.00 ± 0.68	5.14 ± 0.34

Organ uptake values are expressed as %ID/g of tissue except for tumor/blood. Values are mean ± SD; $n = 5$.

activity, and the intratumoral distribution of ^{125}I-IPOS corresponded to the hypoxic regions. These findings demonstrate the feasibility of ^{123}I-IPOS as an imaging probe for HIF-1-active, hypoxic tumors. ^{123}I-IPOS is the first nuclear medical imaging probe for the detection of HIF-1 activity in vivo.

Other hypoxia imaging probes such as ^{18}F-fluoromisonidazole (^{18}F-FMISO) and ^{64}Cu-diacetyl-bis(*N4*-methylthiosemicarbazone) (^{64}Cu-ATSM) have been reported previously. The retention mechanism of both of these probes in the hypoxic regions is based on reduction reactions and the formation of covalent bonds to intracellular macromolecules (*22*). ^{18}F-FMISO uptake is increased only when oxygen levels fall below 2–3 mm Hg (*23*). The uptake of ^{64}Cu-ATSM is also markedly increased in a sigmoidal fashion under hypoxic and anoxic conditions (<3.8 mm Hg) (*24,25*). Previous immunohistochemical study showed that HIF-1α is more frequently present adjacent to blood vessels than in the pimonidazole-positive regions (*26*), and the pO_2 in the HIF-1-active regions is approximately 10–15 mm Hg (*27*). Thus, neither ^{18}F-FMISO nor ^{64}Cu-ATSM is suitable for completely monitoring HIF-1 activity. Recently it was reported that the expression level of HIF-1 correlates with a poor prognosis in many tumors (*8,9*). Thus, imaging HIF-1-active regions in a tumor using ^{123}I-IPOS has the potential to provide insight into those aspects of tumor biology most relevant to treatment design.

Protein transduction with the PTD has proven to be an effective way of delivering proteins in vitro, and recently several reports have also shown valuable in vivo applications for protein transduction in correcting disease states (*28*). A positive charge is important for the cellular membrane permeability of PTD. Moreover, lysine residues are required for efficient ubiquitination and after degradation of HIF-1α (*29*). Therefore, we combined a poly-lysine sequence with a hydrophobic polypeptide to construct a unique PTD, PTD3. We characterized PTD3 in a prior study (*19*).

Because of its extremely high affinity and in vivo stability, we used the SAV-biotin system for radiolabeling the protein. Because the binding of ^{125}I-IBB to POS was inhibited in a concentration-dependent manner by D-biotin (Fig. 2B), it was evident that ^{125}I-IBB bound to the SAV moiety of POS, as was expected. Biotinylated probes have been used for other imaging modalities including fluorescent dyes (*30*) and gadolinium dendrimers (*31*). Thus, POS would have applications not only in nuclear medical imaging but also in optical imaging and MRI.

The luciferase activity in the hypoxic conditions was significantly higher than that in normoxic conditions (Fig. 4A), which indicates that the experimental settings used here to induce hypoxia are suitable for HIF-1α stabilization. After incubation of the cells with ^{125}I-IPOS under normoxic or hypoxic conditions, higher radioactivity was retained in the cells incubated under hypoxic conditions (Fig. 4B), and

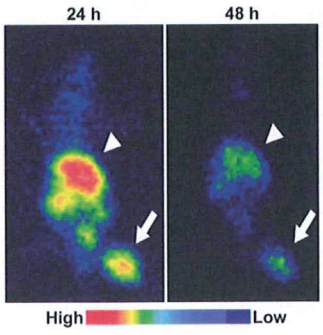

FIGURE 5. Typical planar images of FM3A-implamted mice at 24 or 48 h after injection of ^{123}I-IPOS. Tumors were clearly visualized in both images (arrow). Arrowheads indicate liver.

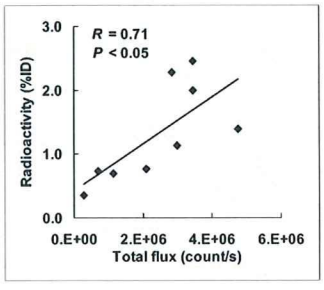

FIGURE 6. Correlation between accumulation of ^{125}I-IPOS and HIF-1 activity within same tumor. Ordinate represents accumulated radioactivity (%ID), and abscissa represents HIF-1-dependent luciferase activity. Correlation coefficient (R) was 0.71, indicating highly significant correlation ($P < 0.05$).

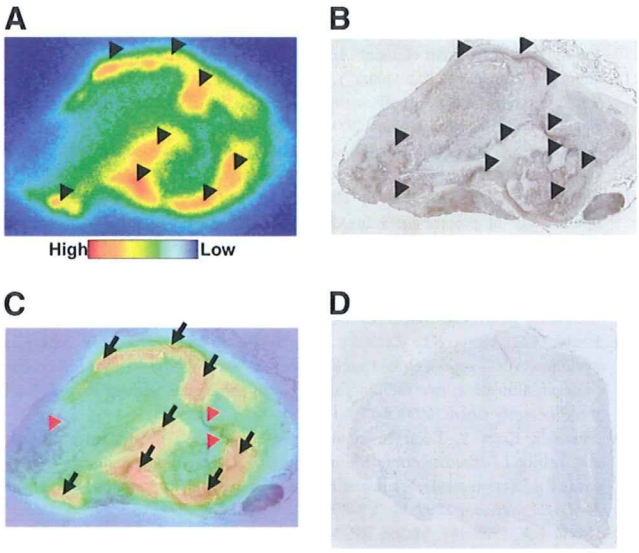

FIGURE 7. Comparison between intratumoral distribution of ^{125}I-IPOS and pimonidazole-positive hypoxic region. Typical autoradiogram (A) and pimonidazole immunohistochemical staining (B) in identical section are shown. Merged image (C) is also presented. Black arrowheads indicate area of ^{125}I-IPOS accumulation in A and pimonidazole-positive area in B. Black arrows show areas in which both signals are positive, and red arrowheads indicate pimonidazole-positive areas without accumulation of ^{125}I-IPOS. No signal was observed in pimonidazole-untreated tumor (D).

intracellular radioactivity under normoxic conditions decreased more rapidly than that under hypoxic conditions (Fig. 4C). The size-exclusion HPLC analysis revealed that the intracellular radioactivity was mostly derived from intact ^{125}I-IPOS and that the radioactivity in the reoxygenated medium was derived from ^{125}I-IBB and other small molecules. Thus, the difference in intracellular radioactivity under normoxic and hypoxic conditions probably reflects the oxygen-dependent degradation of POS, followed by clearance of ^{125}I-IBB from the normoxic cells. Because ^{125}I-IBB is a small molecule and has adequate lipophilicity for membrane transportation, it could be cleared rapidly. However, appreciable radioactivity remained after 24-h incubation under normoxic conditions (Figs. 4B and 4C). Though POS contains the essential domain related to the oxygen-dependent degradation of HIF-1α, it contains PTD and SAV as well. These modifications may lower the rate of degradation.

After injection of ^{125}I-IPOS, high levels of radioactivity were detected in the liver, intestine, and kidneys. Because other constructs incorporating the PTD-ODD fusion proteins or SAV separately did not accumulate in the liver, the fusion of PTD-ODD with SAV may be responsible for hepatic accumulation. Multiple factors, such as molecular size, electrical charge, and slow blood clearance, may be involved. The accumulation in the kidneys may reflect either the propensity of SAV to localize in the kidneys (*32*) or the high HIF-1 activity in the kidneys (*33*). Radioactivity did not accumulate in either the stomach or the thyroid, which demonstrates the resistance of ^{125}I-IPOS to in vivo deiodination. Tumor accumulation of ^{125}I-IPOS increased in a concentration-dependent manner (Table 2). As the administered concentration increased, oxygen-dependent degradation mechanisms in the normal tissues were overwhelmed, thereby increasing the quantity of POS delivered to the tumor.

In vivo imaging revealed that the tumor accumulation of ^{123}I-IPOS correlated with HIF-1 activity. The background radioactivity in the thoracic region was quite low. Thus, ^{123}I-IPOS would be particularly useful for detecting HIF-1 activity in lung and breast tumors. The expression of HIF-1 correlates with a poor prognosis in breast tumors (*34*); therefore, ^{123}I-IPOS may be useful for the noninvasive determination of prognosis.

In the autoradiographic study, there were a few pimonidazole-positive regions in which ^{125}I-IPOS did not accumulate. Regions in which there is no accumulation could be explained by a difference in molecular size. The significantly smaller size of pimonidazole may enable its more efficient delivery to hypoxic tissues than the larger POS. Another possible explanation is the time lag between probe injections. In the present study, ^{125}I-IPOS was injected 22 h before the injection of pimonidazole. The microenvironment in tumors changes dynamically. If the oxygen level of a normoxic region decreased after the degradation of ^{125}I-IPOS, pimonidazole would be able to accumulate in the region. These explanations also indicate the limitations of ^{123}I-IPOS. The slow kinetics due to its molecular size and the necessity of prolonged time for degradation will prevent imaging of acute hypoxic regions with ^{123}I-IPOS. However, it should be emphasized that ^{125}I-IPOS mainly accumulated both in the pimonidazole-positive regions and in the regions surrounding them. This result is consistent with the previous results that HIF-1 expresses at higher levels of oxygen than those that allow pimonidazole metabolism and binding (*26*). Thus, the area in which ^{125}I-IPOS accumulates possibly corresponds to the HIF-1-active hypoxic region.

We confirmed the specific localization of the PTD-ODD fusion protein to HIF-1-active cells using optical imaging techniques (*7,12*). We recently constructed a novel optical imaging probe with the PTD-ODD fusion protein. We then successfully used this probe to obtain specific images of HIF-1-active cells in the ischemic brain of the focal stroke mouse model and of subcutaneous tumors in nude mice. These results further strengthen the argument that PTD-ODD fusion proteins including IPOS are efficiently delivered to hypoxic regions and stabilized in HIF-1-active cells.

CONCLUSION

We have developed a POS fusion protein containing the ODD domain of human HIF-1α. POS was degraded in an oxygen-dependent manner and was stabilized in the cells in which HIF-1 was active. Furthermore, ^{123}I-IPOS enabled the clear visualization of the tumor in vivo and its accumulation

correlated with HIF-1 activity in these tumors. These results support a possible role for ^{123}I-IPOS in the imaging of HIF-1-active tumor hypoxia.

ACKNOWLEDGMENTS

We thank Nihon Medi-Physics for providing the ammonium ^{123}I-iodide. We are grateful to Hiroaki Konishi for skilled technical assistance. This study was supported in part by Health Labour Sciences Research Grant for Research on Advanced Medical Technology, from The Ministry of Health, Labour and Welfare of Japan, and a Grant-in-Aid for Exploratory Research (17659010) from The Ministry of Education, Culture, Sports, Science and Technology of Japan.

REFERENCES

1. Vaupel P, Kallinowski F, Okunieff P. Blood-flow, oxygen and nutrient supply, and metabolic microenvironment of human-tumors: a review. *Cancer Res.* 1989;49:6449–6465.
2. Brown JM. Exploiting the hypoxic cancer cell: mechanisms and therapeutic strategies. *Mol Med Today.* 2000;6:157–162.
3. Hockel M, Vaupel P. Tumor hypoxia: definitions and current clinical, biologic, and molecular aspects. *J Natl Cancer Inst.* 2001;93:266–276.
4. Teicher BA. Hypoxia and drug resistance. *Cancer Metastasis Rev.* 1994;13:139–168.
5. Semenza GL. Expression of hypoxia-inducible factor 1: mechanisms and consequences. *Biochem Pharmacol.* 2000;59:47–53.
6. Wenger RH. Cellular adaptation to hypoxia: O_2-sensing protein hydroxylases, hypoxia-inducible transcription factors, and O_2-regulated gene expression. *FASEB J.* 2002;16:1151–1162.
7. Harada H, Kizaka-Kondoh S, Li G, et al. Significance of HIF-1-active cells in angiogenesis and radioresistance. *Oncogene.* 2007;26:7508–7516.
8. Marignol L, Coffey M, Lawler M, Hollywood D. Hypoxia in prostate cancer: a powerful shield against tumour destruction? *Cancer Treat Rev.* 2008;34:313–327.
9. Miyake K, Yoshizumi T, Imura S, et al. Expression of hypoxia-inducible factor-1α, histone deacetylase 1, and metastasis-associated protein 1 in pancreatic carcinoma: correlation with poor prognosis with possible regulation. *Pancreas.* 2008;36:e1–e9.
10. Bruick RK, McKnight SL. A conserved family of prolyl-4-hydroxylases that modify HIF. *Science.* 2001;294:1337–1340.
11. Wang GL, Jiang BH, Rue EA, Semenza GL. Hypoxia-inducible factor 1 is a basic-helix-loop-helix-PAS heterodimer regulated by cellular O_2 tension. *Proc Natl Acad Sci USA.* 1995;92:5510–5514.
12. Harada H, Kizaka-Kondoh S, Hiraoka M. Optical imaging of tumor hypoxia and evaluation of efficacy of a hypoxia-targeting drug in living animals. *Mol Imaging.* 2005;4:182–193.
13. Kizaka-Kondoh S, Inoue M, Harada H, Hiraoka M. Tumor hypoxia: a target for selective cancer therapy. *Cancer Sci.* 2003;94:1021–1028.
14. Harada H, Hiraoka M, Kizaka-Kondoh S. Antitumor effect of TAT-oxygen-dependent degradation-caspase-3 fusion protein specifically stabilized and activated in hypoxic tumor cells. *Cancer Res.* 2002;62:2013–2018.
15. Kageyama Y, Sugiyama H, Ayame H, et al. Suppression of VEGF transcription in renal cell carcinoma cells by pyrrole-imidazole hairpin polyamides targeting the hypoxia responsive element. *Acta Oncol.* 2006;45:317–324.
16. Inoue M, Mukai M, Hamanaka Y, Tatsuta M, Hiraoka M, Kizaka-Kondoh S. Targeting hypoxic cancer cells with a protein prodrug is effective in experimental malignant ascites. *Int J Oncol.* 2004;25:713–720.
17. Schwarze SR, Ho A, Vocero-Akbani A, Dowdy SF. In vivo protein transduction: delivery of a biologically active protein into the mouse. *Science.* 1999;285:1569–1572.
18. Harada H, Kizaka-Kondoh S, Hiraoka M. Mechanism of hypoxia-specific cytotoxicity of procaspase-3 fused with a VHL-mediated protein destruction motif of HIF-1α containing Pro564. *FEBS Lett.* 2006;580:5718–5722.
19. Kizaka-Kondoh S, Itasaka S, Zeng L, et al. Selective killing of hypoxia-inducible factor-1-active cells improves survival in a mouse model of invasive and metastatic pancreatic cancer. *Clin Cancer Res.* In press.
20. Foulon CF, Alston KL, Zalutsky MR. Synthesis and preliminary biological evaluation of (3-iodobenzoyl)norbiotinamide and ((5-iodo-3-pyridinyl)carbonyl)norbiotinamide: two radioiodinated biotin conjugates with improved stability. *Bioconjug Chem.* 1997;8:179–186.
21. Ishino S, Kuge Y, Takai N, et al. ^{99m}Tc-annexin A5 for noninvasive characterization of atherosclerotic lesions: imaging and histological studies in myocardial infarction-prone Watanabe heritable hyperlipidemic rabbits. *Eur J Nucl Med Mol Imaging.* 2007;34:889–899.
22. Krohn KA, Link JM, Mason RP. Molecular imaging of hypoxia. *J Nucl Med.* 2008;49(suppl 2):129S–148S.
23. Rasey JS, Nelson NJ, Chin L, Evans ML, Grunbaum Z. Characteristics of the binding of labeled fluoromisonidazole in cells in vitro. *Radiat Res.* 1990;122:301–308.
24. Lewis JS, McCarthy DW, McCarthy TJ, Fujibayashi Y, Welch MJ. Evaluation of ^{64}Cu-ATSM in vitro and in vivo in a hypoxic tumor model. *J Nucl Med.* 1999;40:177–183.
25. Vavere AL, Lewis JS. Cu-ATSM: a radiopharmaceutical for the PET imaging of hypoxia. *Dalton Trans.* 2007;4893–4902.
26. Sobhanifar S, Aquino-Parsons C, Stanbridge EJ, Olive P. Reduced expression of hypoxia-inducible factor-1α in perinecrotic regions of solid tumors. *Cancer Res.* 2005;65:7259–7266.
27. Jiang BH, Semenza GL, Bauer C, Marti HH. Hypoxia-inducible factor 1 levels vary exponentially over a physiologically relevant range of O_2 tension. *Am J Physiol.* 1996;271:C1172–C1180.
28. Chauhan A, Tikoo A, Kapur AK, Singh M. The taming of the cell penetrating domain of the HIV Tat: myths and realities. *J Control Release.* 2007;117:148–162.
29. Paltoglou S, Roberts BJ. HIF-1α and EPAS ubiquitination mediated by the VHL tumour suppressor involves flexibility in the ubiquitination mechanism, similar to other RING E3 ligases. *Oncogene.* 2007;26:604–609.
30. Ebner A, Marek M, Kaiser K, et al. Application of biotin-4-fluorescein in homogeneous fluorescence assays for avidin, streptavidin, and biotin or biotin derivatives. *Methods Mol Biol.* 2008;418:73–88.
31. Zhu W, Okollie B, Bhujwalla ZM, Artemov D. PAMAM dendrimer-based contrast agents for MR imaging of Her-2/neu receptors by a three-step pretargeting approach. *Magn Reson Med.* 2008;59:679–685.
32. Forster GJ, Santos EB, Smith-Jones PM, Zanzonico P, Larson SM. Pretargeted radioimmunotherapy with a single-chain antibody/streptavidin construct and radiolabeled DOTA-biotin: strategies for reduction of the renal dose. *J Nucl Med.* 2006;47:140–149.
33. Safran M, Kim WY, O'Connell F, et al. Mouse model for noninvasive imaging of HIF prolyl hydroxylase activity: assessment of an oral agent that stimulates erythropoietin production. *Proc Natl Acad Sci USA.* 2006;103:105–110.
34. Trastour C, Benizri E, Ettore F, et al. HIF-1α and CA IX staining in invasive breast carcinomas: prognosis and treatment outcome. *Int J Cancer.* 2007;120:1451–1458.

Improved Detection of Hepatic Metastases From Pancreatic Cancer Using Periodically Rotated Overlapping Parallel Lines With Enhanced Reconstruction (PROPELLER) Technique After SPIO Administration

Yuusuke Hirokawa, MD, PhD, Hiroyoshi Isoda, MD, PhD,† Tomohisa Okada, MD, PhD,† Shigeki Arizono, MD,† Kotaro Shimada, MD,† Akira Yamamoto, MD, PhD,† Toshiya Shibata, MD, PhD,† and Kaori Togashi, MD, PhD†*

Objectives: The purpose of this study was to evaluate the detection of hepatic metastases from the pancreatic cancer using different MR imaging methods, including superparamagnetic iron oxide (SPIO)-enhanced fat-saturated T2-weighted imaging with periodically rotated overlapping parallel lines with enhanced reconstruction (PROPELLER) technique.

Materials and Methods: The institutional review board approved this prospective study. Eighty-two patients (mean age, 55 years) underwent different MR imaging with a 1.5-T scanner. Diagnostic performance with receiver operating characteristics (ROC) curves and sensitivity were evaluated for the following image sets: (A) unenhanced images (T1-weighted in-phase and opposed-phase gradient-echo [GRE] images, and fat-saturated T2-weighted turbo spin-echo [TSE] images) that were included in the subsequent image sets, (B) diffusion-weighted images, (C) SPIO-enhanced fat-saturated T2-weighted TSE images with prospective acquisition correction (PACE), (D) SPIO-enhanced T2*-weighted GRE images, and (E) SPIO-enhanced fat-saturated T2-weighted TSE images acquired with PROPELLER and PACE.

Results: The areas under the ROC curves were 0.58 ± 0.05 (mean ± standard errors), 0.81 ± 0.04, 0.70 ± 0.05, 0.80 ± 0.04, and 0.90 ± 0.03, and sensitivity was 0.47, 0.69, 0.56, 0.66, and 0.77 for image sets (A) to (E), respectively, for all lesions. Image set (E) had significantly larger area under the ROC curve for detection of hepatic lesions and higher sensitivity than others.

Conclusions: SPIO-enhanced fat-saturated T2-weighted MR imaging with the PROPELLER technique is more effective for detecting hepatic metastases of pancreatic cancer than diffusion-weighted MR imaging, SPIO-enhanced fat-saturated T2WI without the PROPELLER technique, or SPIO-enhanced T2*-weighted GRE imaging.

Key Words: PROPELLER, superparamagnetic iron oxide (SPIO), magnetic resonance imaging (MRI), hepatic metastases of pancreatic cancer

(*Invest Radiol* 2010;45: 158–164)

Magnetic resonance (MR) imaging with superparamagnetic iron oxide (SPIO) particles is a highly sensitive modality for detecting hepatic metastases,[1,2] and is more sensitive than computed tomography (CT).[3,4] Furthermore, this method was reported to be at least as or more accurate than CT during arterial portography, which was previously considered to be the most sensitive modality.[5–7] As a result, SPIO-enhanced MR imaging is used in some institutions for preoperative screening of hepatic metastases.

However, one report showed that combined image interpretation with diffusion-weighted single-shot echo-planar imaging (EPI) with sensitivity-encoding (SENSE) and T2-weighted turbo spin-echo (TSE) and dual-echo fast gradient-echo (GRE) MR imaging yielded better accuracy for detecting hepatic metastases than SPIO-enhanced MR imaging.[8] This suggests that unenhanced diffusion-weighted EPI with SENSE may replace SPIO-enhanced MR imaging to evaluate hepatic metastases. However, in diffusion-weighted EPI, severe image degradation resulting from artifacts and inferior spatial resolution might reduce image clarity and obscure anatomic detail, and thus limit the detection of abdominal lesions.[8–10] In particular, subcardiac or subphrenic signal loss frequently decreases sensitivity for the detection of hepatic lesions.

The periodically rotated overlapping parallel lines with enhanced reconstruction (PROPELLER) MR technique was recently introduced into clinical practice.[11–17] It is a variant of the radial scan techniques and allows for the correction of in-plane motions by using the data at the k-space center. It has recently been applied to the upper abdomen,[10,18] and improvements in image quality were shown for T2-weighted TSE imaging.[19–21]

These observations led us to hypothesize that SPIO-enhanced fat-saturated T2-weighted TSE imaging with the PROPELLER technique may improve the detection of hepatic metastases compared with diffusion-weighted imaging, SPIO-enhanced T2*-weighted GRE imaging or SPIO-enhanced fat-saturated T2-weighted TSE imaging without the PROPELLER technique. In addition, to our knowledge, no large and prospective studies have conducted with SPIO-enhanced MR imaging for its ability to detect hepatic metastatic lesions. Hence, the purpose of our study was to evaluate the detectability of hepatic metastasis from the pancreatic cancer, using different MR imaging methods, including SPIO-enhanced fat-saturated T2-weighted TSE imaging with PROPELLER method, and to determine whether this technique provides additional diagnostic value.

MATERIALS AND METHODS

The institutional review board approved this prospective study, and written informed consent for enrollment in this study was obtained from all patients prior to the MRI study.

Patients

From January 2007 to April 2008, 107 consecutive patients with pancreatic cancer underwent SPIO-enhanced MR imaging to evaluate focal hepatic lesions. Exclusion criteria were (1) clinical contraindications to MRI or SPIO, (2) inability to provide informed

Received June 16, 2009, and accepted for publication, after revision, November 10, 2009.

From the *Department of Radiology, Otsu Red Cross Hospital, Otsu-city, Shiga, Japan; and †Department of Diagnostic Radiology, Kyoto University Graduate School of Medicine, Kyoto, Japan.

Reprints: Yuusuke Hirokawa, MD, PhD, Department of Radiology, Otsu Red Cross Hospital, 1-1-35, Nagara, Otsu-city, Shiga, Japan, 520–8511. E-mail: yuusuke@kuhp.kyoto-u.ac.jp.

ISSN: 0020-9996/10/4503-0158

consent, and (3) the presence of another known malignancy. Fifteen patients were excluded for the following reasons: 5 had contraindications to MRI because of claustrophobia, pacemaker, or prosthesis; 2 were unable to undergo SPIO because of hepatic insufficiency; 3 were unable to provide informed consent; and 5 had another malignancy (3 colorectal cancer, 1 gastric cancer, and 1 breast cancer). The remaining of 92 patients underwent hepatic SPIO-enhanced MR imaging for screening metastases from pancreatic cancer. The diagnosis of pancreatic cancer was confirmed by histologic findings of surgically resected specimens or surgically performed biopsies in 43 patients, cytologic findings of samples collected in endoscopy examinations in 35 patients, and the clinical courses and typical image findings in the remaining 14 patients. Ten patients were excluded for the following reasons: final diagnosis not established (n = 3), or the presence of more than 10 hepatic lesions (n = 7). Therefore, data for 82 patients (mean age, 55 years; range, 32–85 years), including 43 males (mean age, 52 years; range, 32–78 years) and 39 females (mean age, 58 years; range, 36–85 years), were analyzed in the study.

Eligibility of hepatic metastases from pancreatic cancer was obtained as follows. First, hepatic metastases from pancreatic cancer were pathologically diagnosed. If surgery was not performed, the hepatic lesions were diagnosed by the interval growth on images and clinical courses. Hepatic lesions were excluded if they were not pathologically diagnosed post operation or proved difficult to diagnose from the interval evaluation or clinical courses.

MR Image Acquisition and Preparation

The patients underwent upper abdominal MRI examinations using a 1.5-T system (Magnetom Symphony; Siemens Medical Systems, Erlangen, Germany) equipped with a six-channel body phased-array coil. MR imaging with different image contrasts was performed and grouped into (A) to (E), as specified below (summarized in Table 1). Before administration of SPIO (Resovist; Bayer Schering Pharma, Osaka, Japan), fat-saturated T2-weighted TSE imaging, and T1-weighted gradient-echo GRE imaging with dual-echo of in- and opposed-phases were acquired and grouped in the basic image set (A), which was also included in the other image sets from (B) to (E). For the basic image set (A), fat-saturated T2-weighted TSE imaging was conducted with the following parameters: repetition time/echo time (TR/TE), 5330/103 milliseconds; echo train length (ETL), 29; echo train spacing (ETS), 6.4 milliseconds; matrix size, 154 × 256; number of slices, 24; acquisition time, 27 seconds during 2 separate breath-holds at end-expiration. T1-weighted GRE imaging was performed with the following parameters: TR/TE in-phase/TE opposed-phase, 204/4.8/2.4 milliseconds; flip angle (FA), 80 degrees; matrix size, 195 × 256; number of slices, 24; acquisition time, 17 seconds during a breath-hold at end-expiration. Subsequently, diffusion-weighted imaging was conducted with respiration triggering using the prospective acquisition correction (PACE) method before SPIO administration and assigned to image set (B). The parameters were as follows: TR/TE, 1780–3220/91 milliseconds; b factors, 0, 500, and 1000 seconds/mm^2; generalized auto-calibrating partially parallel acquisition (GRAPPA) factor, 2; matrix size, 106 × 128; number of slices, 30; average acquisition time, 173 ± 33 seconds in average.

After the acquisition of image sets (A) and (B), SPIO was administered at a dose of 0.016 mL [8 μmol of iron] per kilogram body weight (maximum: 1.4 mL), which was immediately followed by a saline flush. Over 10 minutes after injection, fat-saturated T2-weighted TSE imaging, T2*-weighted GRE imaging, and fat-saturated T2-weighted TSE imaging with the PROPELLER method were conducted and assigned to image sets of (C), (D), and (E), respectively. For image set (C), fat-saturated T2-weighted TSE imaging was performed under respiration triggering using PACE with the following parameters: TR/TE, 3448–6889/85 milliseconds; ETL, 31; ETS, 5.3 milliseconds; matrix size, 256 × 256; number of slices, 27; average acquisition time, 234 ± 47 seconds in average. For image set (D), T2*-weighted GRE images were acquired first with the following parameters: TR/TE, 169/9 milliseconds; FA, 60 degrees; matrix size, 179 × 256 with reduced field-of-view in the former direction by 80%[8]; number of slices, 24; acquisition time, 48 seconds during 2 separate breath-holds at end-expiration. For image set (E), fat-saturated T2-weighted images were acquired with both PROPELLER and PACE methods with the following parameters: TR/TE, 3462–6766/85 milliseconds; ETL, 31; ETS, 5.3 milliseconds; number of blades, 14; matrix size, 256 × 256; number of slices, 27; average acquisition time, 305 ± 58 seconds. All imaging covered the whole liver with transverse slices of 6 mm thickness with a gap of 1 mm in most cases. Slice thickness, slice gap and field of view were occasionally modified, dependent on the size of the body and the liver, but they were changed in all sequences compared and the effect of changing them is shared among all sequences. The order of sequences was conducted randomly among pre or postcontrast MR imagings.

TABLE 1. Sequences of the 5 MR Image Sets

	Image Sets				
Sequences	**A**	**B**	**C**	**D**	**E**
Non-SPIO-enhanced sequences					
T1-weighted GRE (in-phase and opposed-phase)	○	○	○	○	○
Fat-saturated T2-weighted TSE	○	○	○	○	○
Diffusion-weighted imaging*		○			
SPIO-enhanced sequences					
Fat-saturated T2-weighted TSE without PROPELLER*			○		
T2*-weighted GRE				○	
Fat-saturated T2-weighted TSE with PROPELLER*					○

The sequences used for imaging sets are indicated with circles. *Diffusion-weighted imaging and fat-saturated T2-weighted TSE imaging with and without PROPELLER were conducted with PACE. SPIO indicates super-paramagnetic iron oxide; GRE, gradient echo; TSE, turbo spin echo; PACE, prospective acquisition correction; PROPELLER, periodically rotated overlapping parallel lines with enhanced reconstruction.

Image Data Analysis

One abdominal radiologist (Y.H.; with 13 years of experience) removed any information related to the patient or examination method to avoid giving bias to evaluators. He did not participate in the data analysis. He attended the assessment and presented all image data sets (5 image sets for 82 patients) in a randomized order to evaluators, who were blinded to the aforementioned information. Any 2 image sets from a subject was presented at intervals of more than 4 weeks to minimize possible case memorization. All images sets were presented at random and were evaluated independently by 3 experienced abdominal radiologists (H.I., S.A., and K.S.; with 21, 9, and 9 years of experience, respectively) with a Digital Imaging and Communications in Medicine viewer (Centricity, version 2.0; GE Healthcare BioSciences, Tokyo, Japan). Each evaluator independently checked the presence of hepatic lesions on the basis of a 5-point confidence scale: 1, definitely or almost definitely absent; 2, probably absent; 3, possibly present; 4, probably present; and 5, definitely or almost definitely present. The evaluators also noted the segments in which they founded the suspected hepatic lesions. If